Article

Not peer-reviewed version

Petrogenesis and Tectonic Setting of the Late Permian Granitoid in the East Kunlun Orogenic Belt, NW China: Constraints from Petrology, Geochemistry and Zircon U-Pb-Lu-Hf Isotopes

Chao Hui , Fengyue Sun * , Tao Wang , Yanqian Yang , Yun Chai , Jiaming Yan , Bakht Shahzad , Bile Li , Yajing Zhang , Tao Yu , Xingsen Chen , Chengxian Liu , Xinran Zhu , Yuxiang Wang , Zhengsong Wang , Haoran Li , Renyi Song , Desheng Dou

Posted Date: 18 February 2025

doi: 10.20944/preprints202502.1347.v1

Keywords: east Kunlun orogenic belt; Permian granitoids; Paleo-Tethys Ocean; slab roll-back; tectonic evolution

doi:10.20944/preprints202502.1347.v1

Article

Petrogenesis and Tectonic Setting of the Late Permian Granitoid in the East Kunlun Orogenic Belt, NW China: Constraints from Petrology, Geochemistry and Zircon U-Pb-Lu-Hf Isotopes

Chao Hui [1], Fengyue Sun [1,2,*], Tao Wang [3,4], Yanqian Yang [3,4], Yun Chai [3,4], Jiaming Yan [1], Bakht Shahzad [1], Bile Li [1,4], Yajing Zhang [1], Tao Yu [5], Xingsen Chen [1], Chengxian Liu [1], Xinran Zhu [1], Yuxiang Wang [1], Zhengsong Wang [1], Haoran Li [1], Renyi Song [1] and Desheng Dou [1]

1 College of Earth Sciences, Jilin University, Changchun 130061, China
2 Key Laboratory of Mineral Resources Evaluation in Northeast Asia, Ministry of Natural Resources of China, Jilin University, Changchun 130061, China
3 Qinghai Geological Survey, Xining 810000, China
4 Technology Innovation Center for Exploration and Exploitation of Strategic Mineral Resources in Plateau Desert Region, Ministry of Natural Resources, Xining 810000, China
5 Northeast Oli & Gas branch of SINOPEC, Changchun 130062, China
* Correspondence: fengyue_sun@163.com

Abstract: Permian magmatic rocks are extensively distributed in the East Kunlun Orogenic Belt (EKOB), yet controversies persist regarding the petrogenesis of granitoid and the tectonic evolution of the Buqingshan-A'nyemaqing Ocean (BAO), a Paleo-Tethys oceanic branch. This study addresses these debates through petrological analyses, whole-rock geochemistry, and zircon U-Pb-Lu-Hf isotopic investigations of newly identified granitoids in the EKOB. The monzogranite (MG) and quartz porphyry (QP) yield weighted mean ages of 254.7 ± 1.1 Ma and 254.3 ± 1.1 Ma, respectively. Geochemically, the MG shows metaluminous to weakly peraluminous low-K calc-alkaline I-type granites, characterized by high SiO_2, low K_2O, MgO, FeO^T contents, and marked enrichment in light rare earth elements (LREEs), but depletion in Eu, Ba, Sr, P and Ti anomalies. In contrast, the QP exhibits peraluminous high-K calc-alkaline I-type affinities, displaying high SiO_2 but low Na_2O and P_2O_5 contents. It is enriched in LREEs and Rb but displays negative Nb, Sr, P, and Ti anomalies. Zircon $\varepsilon_{Hf}(t)$ values range from −1.6 to 2.6 (MG) and −4.4 to 1.5 (QP). We suggest the MG and QP are derived from the partial melting of the juvenile mafic lower crust, and the MG has undergone highly fractional crystallization. Synthesis of multiscale geological evidence allows us to delineate a five-stage tectonic evolution for the BAO in the EKOB: (1) oceanic basin initiation prior to ca. 345 Ma; (2) incipient northward subduction commencing at ca. 278 Ma; (3) slab roll-back stage (263–240 Ma); (4) syn-collisional compression (240–230 Ma); and (5) post-collisional extension (230–195 Ma).

Keywords: east Kunlun orogenic belt; Permian granitoids; Paleo-Tethys Ocean; slab roll-back; tectonic evolution

1. Introduction

The east Kunlun orogenic belt (EKOB), a prototype subduction-accretion orogen, preserves multistage tectonomagmatic records, associated with Cambrian-Devonian Proto-Tethys and Carboniferous-Triassic Paleo-Tethys oceanic cycles [1–10]. While consensus exists on the Paleo-Tethyan oceanic opening prior to the Early Carboniferous [11–13] and initial northward subduction around 278 Ma [14]. Three principal controversies persist regarding its geodynamic evolution: (1) Majority view: Prolonged subduction (278–240 Ma) followed by collisional (240–230 Ma) and post-

 doi:10.20944/preprints202502.1347.v1

collisional phases (230–190 Ma) [3,5,7,8,15–17]. (2) Alternative model 1: Early collision initiation (pre-251 Ma) transitioning to post-collisional extension by 247Ma [18,19]. (3) Alternative model 2: Continuous subduction through the Late Triassic prior to terminal collision [20–22]. Petrogenetic investigations of EKOB granitoids document diverse magma provenance systems, including: (1) Subducted oceanic plate with overlying sedimentary [18,23], (2) lower crust [4,24], (3) juvenile mafic crust [25,26], (4) enriched mantle [27,28], (5) hybrid mantle-crust systems [29,30].

To address these debates, we conducted an integrated petrogenetic investigation of two Permian granitoids (monzogranite and quartz porphyry) from the Xingshugou area within EKOB. Through combined petrological analysis, whole-rock geochemistry, zircon U-Pb geochronology, and in-situ zircon Hf isotopic studies, this work aims to: (1) Constrain the magmatic sources and petrogenetic processes, (2) reconstruct the Paleo-Tethyan geodynamic evolution during critical Permian–Triassic transition.

2. Geological Setting and Samples

2.1. Regional Geology

The EKOB, situated along the northern margin of the Tibet Plateau in northwest China (Figure 1a), is bounded by four principal tectonic domains: the Qaidam Block to the north, the A'nyemaqen ophiolitic belt (AOB) to the south, the Altyn Tagh strike-slip fault system to the west, and the Wenquangou-Wahongshan fault to the east (Figure 1b). This orogen expends approximately 1,500 km in an E-W direction with a width of 50–200 km [2,22]. The Wutumeiren Township divides the EKOB into western and eastern sectors [31]. The EKOB is subdivided into three belts, which are the Caledonian back-arc basin of Northern East Kunlun Orogenic Belt (NKB), uplifted granitic basement of Central East Kunlun Orogenic Belt (CKB), and composite accretion of the Southern East Kunlun Orogenic Belt (SKB) from north to south, respectively (Figure1 b). The boundaries of them are northern east Kunlun fault (NEKF, also named as Nalinggele Fault in the western EKOB), central east Kunlun fault (CEKF), and southern east Kunlun fault (SEKF) from north to south, respectively (Figure1 b) [2,32]. The basement compositions exhibit spatial heterogeneity: (1) the NKB and CKB are Paleo-proterozoic Jinshuikou Group, (2) while the SKB is Meso- to Neo-proterozoic Wanbaogou basaltic oceanic plateau, which was produced by a mantle plume [32]. The EKOB records a protracted tectonic evolution involving (1) Cambrian–Devonian Proto-Tethys Ocean and Carboniferous–Triassic Paleo-Tethys Ocean [2,3,5,6,11,22,32,33]. Notably, Phanerozoic granitoids cover an area of approximately 47,500km^2, with Permian–Triassic granitoids accounting for 23,000km^2 (approximately 48% of total exposure) [31].

Preprints.org (www.preprints.org) | NOT PEER-REVIEWED | Posted: 18 February 2025 doi:10.20944/preprints202502.1347.v1

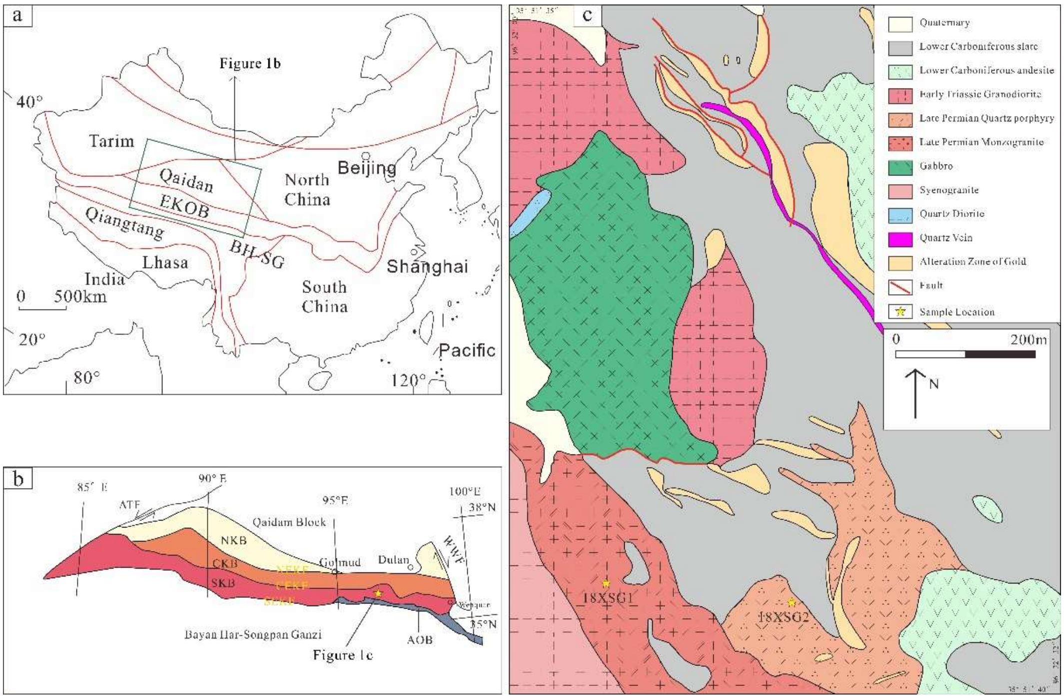

Figure 1. (a) Simplified tectonic map of China (after [34]), (b) Outline of tectonic map of the EKOB showing the three major faults and tectonic belts (modified from [2,32]), (c) Geological map of Xingshugou area and sample location. ATF: Altyn Tagh strike-slip fault, WWF: Wenquangou-Wahongshan fault, NEKF: northern east Kunlun fault, CEKF: central east Kunlun fault, SEKF: southern east Kunlun fault, NKB: Caledonian back-arc basin Belt of Northern East Kunlun, CKB: uplifted granitic basement of Central East Kunlun, SKB: composite accretion belt of the Southern East Kunlun, AOB: A'nyemaqen ophiolitic belt.

2.2. Geology of Study Area

The Xingshugou (XSG) study area is situated within the SKB, approximately 70 km south of Nuomuhong Township (Figure 1b). The region exposes a complex intrusive suite dominated by granodiorite, monzogranite, quartz porphyry and gabbro, with subordinate moyite. These plutons intrude the Lower Carboniferous Halaguole Formation, which comprises andesite sequences interbedded with carbonaceous slate (Figure 1c). Structural analysis reveals two predominant fault systems: (1) NW-SE trending and E-W oriented primary faults, and (2) secondary N-S trending fractures (Figure 1c). Notably, the magmatic complex is spatially associated with an epithermal low-sulfidation Au deposit (Figure 1c), suggesting potential genetic links between magmatism and hydrothermal mineralization.

2.3. Sample Descriptions

Two representative granitoid samples were systematically collected from XSG magmatic complex (Figure 1c).

(1) Monzogranite (MG), which was collected at 96°32′07″E, 35°51′07″N (Figure 1c), is flesh-pink and fine- to medium-grained granitic texture. It consists of plagioclase (~ 30 vol.%), potassium feldspar (~ 25 vol.%), quartz (~ 40 vol.%), biotite (< 5 vol.%), and accessory minerals including apatite, zircon, and opaque minerals (Figure 2a, b).

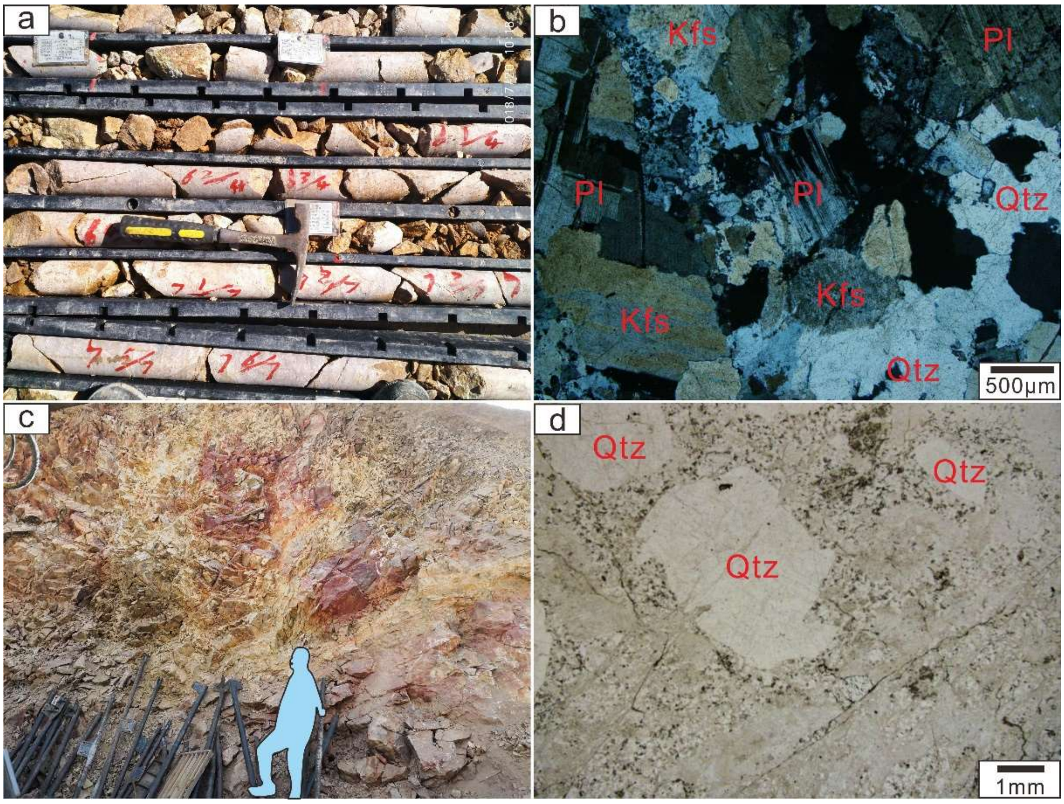

Figure 2. The field photographs and photomicrographs of monzogranite (a, b) and quartz porphyry (c, d). Qtz: quartz, Pl: plagioclase, Kfs: K-feldspar.

(2) Quartz porphyry (QP), which was collected at 96°32′17″E, 35°51′07″N (Figure 1c), is light gray and porphyritic texture. The phenocrysts are potassium feldspar (~ 10 vol.%), plagioclase (~ 10 vol.%), and quartz (~ 10 vol.%), the groundmass consists of plagioclase (~ 20 vol.%), K-feldspar (~ 20 vol.%), quartz (~ 20 vol.%), biotite (< 5 vol.%), and accessory minerals including apatite, zircon and opaque minerals (Figure 2c, d).

3. Analytical Methods

3.1. Zircon U-Pb Dating

Zircons were separated and selected for dating at Langfang Tuoxuan Rock and Mineral Testing Service Co., Ltd., Langfang, China, through the methods of heavy liquid and electromagnetic sorting combined with hand selection under the stereobinocular microscope. Then, an epoxy resin target was made for imaging in transmitted-reflected light and cathodoluminescence (CL). Zircon U-Pb isotope and trace elements were carried out at Yanduzhongshi Geological Analysis Laboratories Ltd., Langfang, China, by using an NWR193 laser-ablation microprobe (Elemental Scientific Lasers LLC), attached to an Analytikjena PlasmaQuant MS quadrupole ICP-MS. In this test, the diameter of the ablation spot is 32 μm. Detailed analytical methods were reported by [15], Data analytical ICP-MS-DATACAL program was used to calculate the isotopic data [35,36]. ISOPLOT toolkit for Microsoft Excel was used to calculate the weighted average ages and plot the concordia diagram [37].

3.2. Whole-Rock Major and Trace Elements Analyses

Major and trace elements of whole rock were conducted at the Key Laboratory of Mineral Resources Evaluation in Northeast Asia, Ministry of Natural Resources of China, Jilin University. Fresh samples were powdered to 200 mesh by an agate ring mill. Major elements were analyzed by X-ray fluorescence (XRF) spectrometer. For trace elements analyses, samples were digested by HF + HNO_3 in Teflon bombs, then analyzed with an Agilent 7500a inductively coupled plasma mass spectrometry (ICP-MS). The precision for major and trace elements is better than 1% and 5%, respectively.

3.3. Zircon In Situ Lu-Hf Isotope Analyses

Zircon in situ Lu-Hf isotope analysis was carried out at Yanduzhongshi Geological Analysis Laboratories Ltd., Beijing, China. By using a NWR193 laser-ablation microprobe (Elemental Scientific Lasers LLC) attached to a Neptune multi-collector ICP-MS. The size of the laser beam spot is 38 μm in diameter. In situ Hf isotope analyzed position was the same spots as the U-Pb dating. Detailed analytical and data processing methods are presented by [15] and [38].

4. Results

4.1. Zircon U-Pb Dating

Zircon crystals from samples MG (18XSG1) and QP (18XSG2) exhibit transparent, light brown and euhedral morphologies (80–200 μm) with well-developed prismatic faces and oscillatory zoning in CL images (Figure 3c, f). High Th/U ratios (0.28–5.39) confirm their magmatic origin [39]. The zircon U-Pb isotopic data is presented in Table 1. Zircon U-Pb concordia $^{206}Pb/^{238}U$ ages of MG and QP yield 254.7 ± 0.57 Ma (MSWD = 0.26, n = 26) (Figure 3a) and 254.3 ± 0.57 Ma (MSWD = 0.035, n = 26) (Figure 3d), respectively. Zircon U-Pb weighted mean $^{206}Pb/^{238}U$ ages of MG and QP yield 254.7 ± 1.1 Ma (MSWD = 0.26, n = 26) (Figure 3b) and 254.3 ± 1.1 Ma (MSWD = 0.116, n = 26) (Figure 3e), respectively. Therefore, the crystallization timing of both intrusions is the Late Permian.

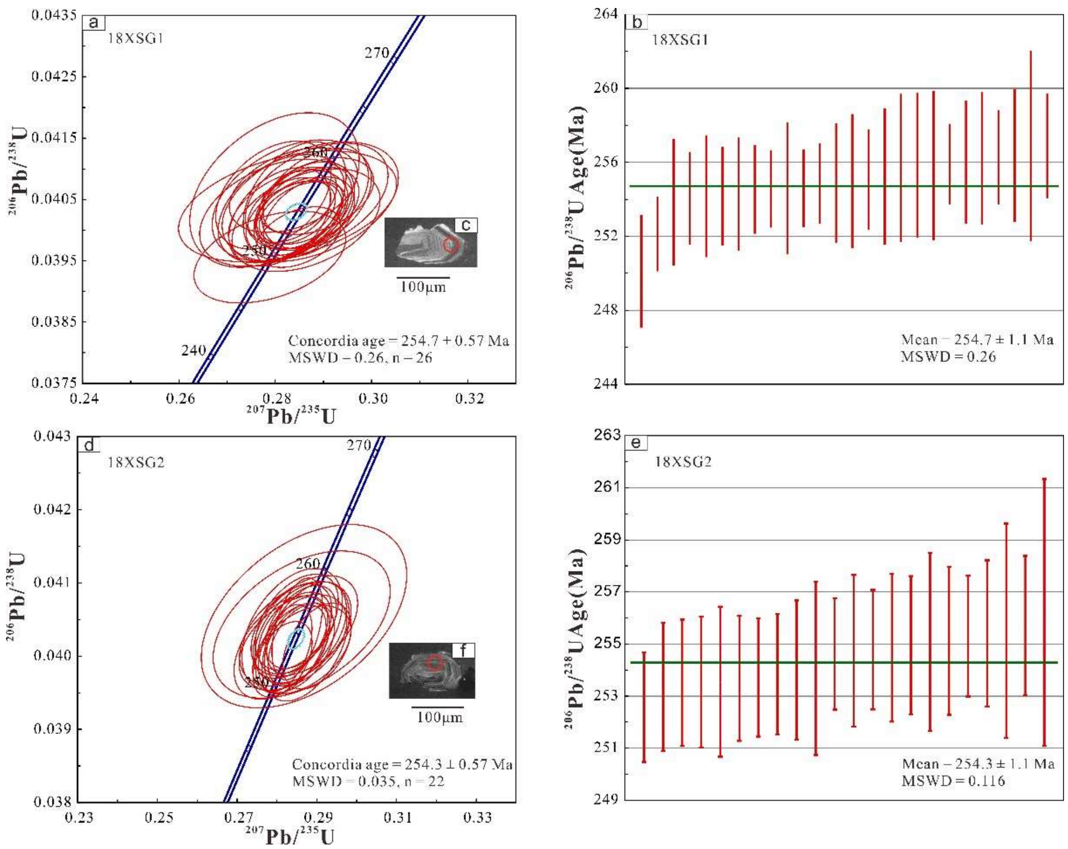

Figure 3. Zircon U-Pb concordia diagrams, weighted mean age diagrams and representative zircon CL images for samples. (a–c) Monzogranite (18XSG1); (d–f) quartz porphyry (18XSG2).

Preprints.org (www.preprints.org) | NOT PEER-REVIEWED | Posted: 18 February 2025 doi:10.20944/preprints202502.1347.v1

Table 1. LA-ICP-MS U-Pb isotopic data for zircons for Xingshugou monzogranite (18XSG1) and quartz porphyry (18XSG2).

Sample Name	Content (ppm)				Isotopic ratios						Isotopic ages (Ma)					
	U	Th	Pb	Th/U	$^{207}Pb/^{206}Pb$	1σ	$^{207}Pb/^{235}U$	1σ	$^{206}Pb/^{238}U$	1σ	$^{207}Pb/^{206}Pb$	1σ	$^{207}Pb/^{235}U$	1σ	$^{206}Pb/^{238}U$	1σ
18XSG1-monzogranite, weighted mean age: 254.7 ± 1.1 Ma, MSWD = 0.26																
18XSG11-1	136	169	8	1.25	0.05140	0.00192	0.27890	0.01040	0.03956	0.00049	258.71648	85.75895	249.78293	8.25463	250.10093	3.06022
18XSG11-2	272	309	15	1.14	0.05199	0.00109	0.28480	0.00581	0.03989	0.00033	284.81419	47.85650	254.45604	4.59370	252.12208	2.01725
18XSG11-3	250	302	14	1.21	0.05211	0.00190	0.28639	0.01016	0.04016	0.00055	290.31512	83.26791	255.71640	8.01661	253.84337	3.42558
18XSG11-4	245	298	14	1.22	0.05164	0.00128	0.28393	0.00657	0.04020	0.00040	269.32848	56.90187	253.77020	5.19438	254.04809	2.50053
18XSG11-5	433	478	24	1.10	0.05084	0.00117	0.28095	0.00696	0.04021	0.00053	233.45662	53.10910	251.41094	5.51512	254.15459	3.29228
18XSG11-6	377	377	20	1.00	0.05193	0.00107	0.28701	0.00624	0.04021	0.00043	282.41105	47.03537	256.20248	4.92545	254.15973	2.65871
18XSG11-7	216	222	12	1.03	0.05150	0.00165	0.28270	0.00820	0.04023	0.00049	263.41689	73.36666	252.79409	6.48970	254.27459	3.05476
18XSG11-8	363	429	20	1.18	0.05153	0.00112	0.28503	0.00600	0.04027	0.00039	264.59209	49.92739	254.63626	4.73928	254.53441	2.39550
18XSG11-9	311	381	18	1.23	0.05163	0.00115	0.28569	0.00593	0.04028	0.00034	269.21598	51.21303	255.16324	4.68715	254.56553	2.09772
18XSG11-10	351	363	18	1.03	0.05048	0.00180	0.28014	0.01045	0.04028	0.00058	217.07634	82.60975	250.76554	8.28831	254.58830	3.57059
18XSG11-11	322	448	19	1.39	0.05149	0.00104	0.28413	0.00549	0.04029	0.00034	262.61823	46.40960	253.92821	4.34425	254.60255	2.09825
18XSG11-12	347	491	21	1.42	0.05102	0.00100	0.28297	0.00570	0.04033	0.00035	241.61252	45.39917	253.00693	4.50891	254.85231	2.16833
18XSG11-13	303	303	16	1.00	0.05172	0.00129	0.28600	0.00688	0.04033	0.00052	273.23716	57.01755	255.40424	5.43600	254.86556	3.22598
18XSG11-14	277	271	15	0.98	0.05060	0.00141	0.28129	0.00866	0.04035	0.00058	222.55786	64.31826	251.68285	6.86413	254.99052	3.61131
18XSG11-15	432	531	24	1.23	0.05167	0.00123	0.28679	0.00699	0.04036	0.00044	270.91240	54.51252	256.03325	5.51555	255.07438	2.70824
18XSG11-16	219	256	12	1.17	0.05085	0.00271	0.28257	0.01494	0.04039	0.00060	233.94178	122.80923	252.69145	11.83102	255.23405	3.69472
18XSG11-17	266	332	15	1.25	0.05170	0.00220	0.28728	0.01208	0.04046	0.00065	272.18221	97.36731	256.41435	9.52978	255.69555	3.99674
18XSG11-18	2214	1479	112	0.67	0.05077	0.00118	0.28405	0.00706	0.04048	0.00063	230.32009	53.50437	253.86754	5.58259	255.82961	3.90924
18XSG11-19	258	308	14	1.19	0.05059	0.00171	0.28314	0.01071	0.04048	0.00065	222.30992	77.94628	253.14426	8.47522	255.83191	4.03556
18XSG11-20	284	334	16	1.18	0.05119	0.00099	0.28513	0.00504	0.04049	0.00035	249.51167	44.49065	254.71927	3.98139	255.89568	2.18967
18XSG11-21	270	275	15	1.02	0.05173	0.00128	0.28864	0.00750	0.04051	0.00054	273.27247	56.80927	257.48545	5.91149	256.01441	3.33372
18XSG11-22	247	279	14	1.13	0.05180	0.00171	0.28863	0.00978	0.04054	0.00058	276.62797	75.54745	257.47784	7.70645	256.20665	3.57857
18XSG11-23	192	216	11	1.13	0.05169	0.00142	0.28860	0.00783	0.04055	0.00041	271.84486	63.17471	257.45876	6.16958	256.26289	2.55778
18XSG11-24	237	242	13	1.02	0.05031	0.00146	0.27965	0.00791	0.04057	0.00058	209.12693	67.14474	250.37762	6.27272	256.36658	3.59743
18XSG11-25	253	342	14	1.35	0.05013	0.00220	0.27987	0.01161	0.04065	0.00083	200.79700	101.82341	250.55223	9.21420	256.88298	5.15797
18XSG11-26	339	520	21	1.53	0.05086	0.00163	0.28376	0.00878	0.04065	0.00046	234.69723	74.06923	253.63532	6.94197	256.88476	2.82308
18XSG2-quartz porphyry, weighted mean age: 254.3 ± 1.1 Ma, MSWD = 0.116																
18XSG21-1	622	315	29	0.51	0.05108	0.00082	0.28144	0.00490	0.03996	0.00034	244.62329	37.16388	251.79940	3.88583	252.56887	2.10306
18XSG21-2	404	558	24	1.38	0.05184	0.00155	0.28623	0.00814	0.04008	0.00040	278.41178	68.55784	255.59015	6.42689	253.35592	2.46419

Preprints.org (www.preprints.org) | NOT PEER-REVIEWED | Posted: 18 February 2025 doi:10.20944/preprints202502.1347.v1

18XSG21-3	796	518	40	0.65	0.05098	0.00087	0.28212	0.00444	0.04011	0.00039	240.00655	39.54202	252.33405	3.51374	253.51168	2.42252
18XSG21-4	322	229	16	0.71	0.05155	0.00121	0.28455	0.00654	0.04011	0.00040	265.71394	53.95271	254.25664	5.17224	253.53616	2.50892
18XSG21-5	411	326	21	0.79	0.05088	0.00138	0.28126	0.00792	0.04012	0.00046	235.20489	62.51900	251.65580	6.27676	253.55114	2.87919
18XSG21-6	653	501	34	0.77	0.05240	0.00101	0.29010	0.00568	0.04014	0.00039	302.95284	44.07263	258.64185	4.47002	253.67520	2.40100
18XSG21-7	495	481	26	0.97	0.05156	0.00084	0.28509	0.00482	0.04014	0.00037	265.73063	37.57581	254.68690	3.80942	253.71665	2.27398
18XSG21-8	548	155	25	0.28	0.05132	0.00087	0.28504	0.00544	0.04016	0.00037	255.37216	38.99096	254.64898	4.29857	253.83307	2.31534
18XSG21-9	399	294	21	0.74	0.05114	0.00156	0.28403	0.00892	0.04019	0.00043	247.17875	70.42622	253.84980	7.05674	254.00163	2.67342
18XSG21-10	491	431	25	0.88	0.05169	0.00125	0.28724	0.00721	0.04020	0.00054	271.71940	55.27211	256.38561	5.68736	254.06274	3.32777
18XSG21-11	570	528	31	0.93	0.05137	0.00081	0.28510	0.00507	0.04029	0.00035	257.53897	36.37910	254.69304	4.00320	254.61519	2.13993
18XSG21-12	169	108	8	0.64	0.05172	0.00162	0.28464	0.00923	0.04031	0.00047	273.25698	71.91713	254.32936	7.29228	254.73663	2.91313
18XSG21-13	406	370	22	0.91	0.05126	0.00109	0.28449	0.00603	0.04031	0.00037	252.75751	48.75249	254.21339	4.76385	254.77976	2.29346
18XSG21-14	479	523	27	1.09	0.05148	0.00137	0.28600	0.00760	0.04033	0.00046	262.20087	60.97490	255.40573	6.00082	254.85345	2.83598
18XSG21-15	374	285	19	0.76	0.05098	0.00107	0.28395	0.00654	0.04034	0.00043	239.75846	48.33665	253.78688	5.16854	254.94869	2.65390
18XSG21-16	266	158	13	0.60	0.05093	0.00143	0.28384	0.00832	0.04036	0.00055	237.65258	64.53973	253.70299	6.58242	255.07761	3.41664
18XSG21-17	837	540	42	0.65	0.05114	0.00073	0.28510	0.00417	0.04037	0.00046	247.32116	33.06678	254.69482	3.29436	255.12577	2.84464
18XSG21-18	603	468	31	0.78	0.05114	0.00086	0.28604	0.00587	0.04040	0.00037	247.13819	38.88435	255.43923	4.63591	255.29862	2.31669
18XSG21-19	277	289	15	1.04	0.05160	0.00153	0.28690	0.00883	0.04041	0.00045	267.91562	67.81175	256.11619	6.96804	255.39846	2.81089
18XSG21-20	67	62	4	0.92	0.05213	0.00282	0.28623	0.01467	0.04043	0.00066	291.01991	123.70139	255.58632	11.57792	255.50768	4.11349
18XSG21-21	361	298	19	0.82	0.05114	0.00120	0.28502	0.00688	0.04046	0.00043	247.08752	54.01408	254.63222	5.43348	255.70845	2.67330
18XSG21-22	45	241	5	5.39	0.05249	0.00310	0.28681	0.01701	0.04054	0.00083	306.83536	134.44840	256.04430	13.42563	256.20864	5.12164

Preprints.org (www.preprints.org) | NOT PEER-REVIEWED | Posted: 18 February 2025 doi:10.20944/preprints202502.1347.v1

4.2. Major And Trace Elements

The data of major and trace elements is presented in Table 2.

4.2.1. Monzonitic Granite (MG)

The MG shows high SiO_2 (73.00 - 79.56 wt%) contents, but low K_2O (0.31–3.97 wt%), TiO_2 (0.08–0.21 wt%), FeO^T (FeO^T = FeO + Fe_2O_3 * 0.8998, 1.01–1.76 wt%), MnO (0.02–0.06 wt%), P_2O_5 (0.01–0.05 wt%) and MgO (0.11–0.24 wt%) contents and $Mg^{\#}$ ($Mg^{\#}$ = 100 × molar MgO/(MgO + FeO^T), 12.71–19.99) (Figure 4b, c). The value of A/CNK (A/CNK = molar Al_2O_3/(CaO + Na_2O + K_2O) ranges from 0.84 to 1.16 (Figure 4d). All of the above suggested the MG was low-K subalkaline metaluminous rock. It is enriched in light rare earth elements (LREEs) with $(La/Yb)_N$ ($(La/Yb)_N$ = $(La_{Sample}/La_{CI})/(Yb_{Sample}/Yb_{CI})$) of 7.07–49.23 (Figure 5a) and large ion lithophile elements (LILEs, such as Rb and Th) (Figure 5b). They also show significant negative Eu anomalies (Eu/Eu* = 0.28–0.32, one outlier at 1.23; Eu/Eu* = (Eu_{Sample}/Eu_{CI})/{[(Sm_{Sample}/Sm_{CI}) * (Gd_{Sample}/Gd_{CI})]^ (1/2)}) (Figure 5a), and depleted in Ba, K, Sr, P, Ti (Figure 5b).

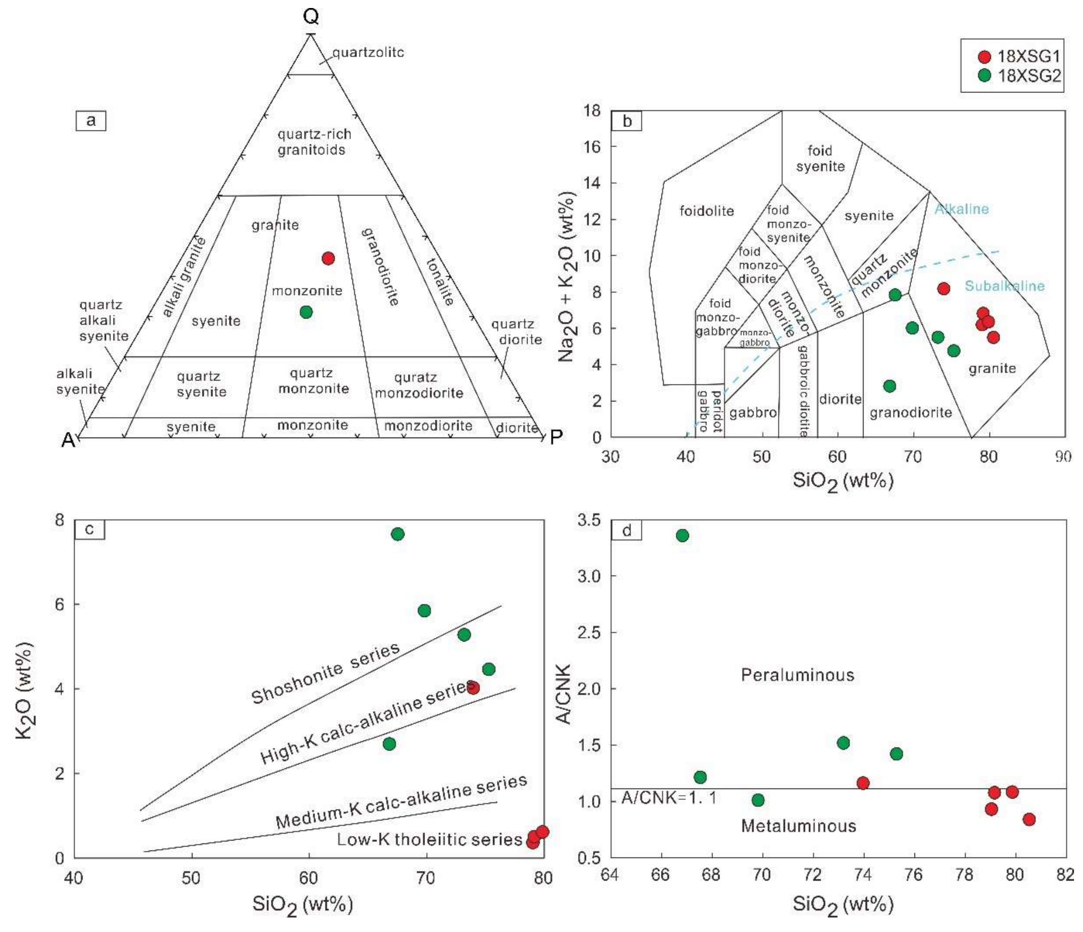

Figure 4. (a) Diagrams of QAP, after [40]; (b) $Na_2O + K_2O$ (wt%) vs. SiO_2 (wt%), after [41]; (c) K_2O vs. SiO_2, after [42]; (d) A/CNK vs. SiO_2.

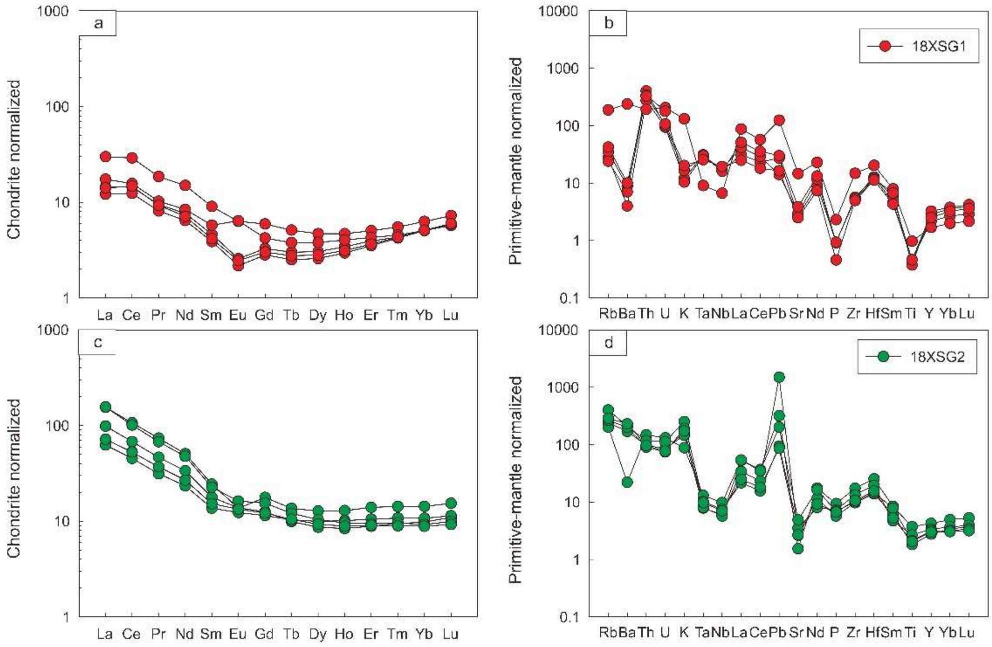

Figure 5. Chondrite-normalized REEs and primitive mantle-normalized trace elements patterns. (a, b) Monzogranite (18XSG1); (c, d) quartz porphyry (18XSG2). Normalization values are from [43].

Table 2. Major(wt%) and trace elements (ppm) data for Xingshugou monzogranite (18XSG1) and quartz porphyry (18XSG2).

Rock type	monzogranite					quartz porphyry				
Sample No.	18XSG1-1	18XSG1-2	18XSG1-3	18XSG1-4	18XSG1-5	18XSG2-1	18XSG2-2	18XSG2-3	18XSG2-4	18XSG2-5
Major elements (wt%)										
SiO_2	78.21	73.00	78.29	79.56	79.01	74.32	65.86	66.68	68.91	72.31
TiO_2	0.10	0.21	0.10	0.08	0.10	0.39	0.81	0.58	0.46	0.45
Al_2O_3	11.65	14.46	12.17	10.49	11.49	11.22	20.20	14.76	12.92	12.95
Fe_2O_3	0.43	1.22	0.40	0.29	0.77	4.00	4.44	2.17	1.67	3.28
FeO	0.81	0.64	0.79	0.73	0.79	1.59	1.45	2.94	3.27	1.85
MnO	0.03	0.06	0.02	0.03	0.03	0.16	0.20	0.21	0.28	0.16
MgO	0.12	0.24	0.11	0.11	0.12	0.78	1.01	1.51	1.69	0.87
CaO	1.45	0.76	0.27	2.05	0.34	1.45	1.61	2.02	3.44	1.38
Na_2O	5.77	4.10	6.24	5.11	5.67	0.29	0.12	0.17	0.16	0.22
K_2O	0.36	3.97	0.50	0.31	0.61	4.40	2.66	7.56	5.77	5.21
P_2O_5	0.02	0.05	0.02	0.02	0.01	0.12	0.20	0.16	0.15	0.15
LOI	0.90	1.25	0.70	1.20	0.85	1.20	1.00	1.10	0.80	1.10
Total	99.86	99.96	99.61	99.99	99.79	99.92	99.57	99.86	99.51	99.90
FeO^T	1.21	1.76	1.16	1.01	1.50	5.25	5.53	4.95	4.83	4.85
$Mg^{\#}$	15.29	19.99	14.69	16.79	12.71	21.25	25.03	35.66	38.92	24.64
A/CNK	0.93	1.16	1.08	0.84	1.08	1.42	3.36	1.21	1.01	1.52
A/NK	1.18	1.31	1.13	1.20	1.15	2.14	6.57	1.74	1.98	2.15
Trace elements (ppm)										
Li	0.25	4.01	2.19	4.02	2.66	21.81	48.51	22.86	14.37	20.46
Be	1.96	1.18	1.58	1.32	1.06	0.87	1.54	0.86	0.89	0.93
B	11.49	18.19	8.33	9.35	6.57	11.76	19.34	14.52	8.98	12.21
Sc	1.09	1.11	2.14	1.81	1.67	7.73	10.27	9.08	7.58	7.56
Ti	537.80	1298.00	564.60	421.40	472.20	2275.00	3990.00	3129.00	2380.00	2497.00
V	3.22	16.18	2.51	3.06	3.65	59.89	92.46	74.28	58.62	64.67
Cr	5.27	6.65	4.08	5.54	3.91	7.70	4.71	4.95	6.34	5.85
Mn	154.80	370.20	103.60	139.40	164.50	1171.00	1327.00	1396.00	1823.00	1075.00
Co	2.86	4.10	3.16	2.25	3.54	10.41	10.14	7.59	87.14	7.46
Ni	2.50	3.13	1.70	2.22	1.32	4.01	3.39	2.77	4.98	3.11
Cu	4.01	36.72	4.03	4.08	3.32	152.00	93.74	516.90	280.10	273.20
Zn	9.70	63.54	7.41	9.01	8.17	163.90	184.50	157.10	112.20	147.50

 doi:10.20944/preprints202502.1347.v1

Ga	7.47	11.05	10.51	10.70	8.87	11.16	17.50	12.54	10.50	11.73
As	7.46	9.82	2.73	3.45	2.06	18.23	13.55	6.61	5.41	8.36
Se	1.14	1.08	1.25	1.22	1.06	1.70	1.76	1.42	1.47	1.48
Rb	17.68	119.50	22.19	15.21	26.93	154.50	127.80	254.90	168.00	182.70
Sr	56.41	309.10	63.22	81.85	52.61	55.72	32.52	74.41	103.40	56.50
Y	9.83	7.67	13.03	14.79	11.42	12.58	19.36	15.37	14.42	13.64
Zr	63.48	165.60	62.83	59.17	55.76	109.10	194.90	149.40	113.30	120.00
Nb	11.56	4.74	12.39	11.46	13.83	4.29	6.95	5.30	4.06	5.01
Mo	5.49	1.50	0.50	0.84	3.10	1.42	5.32	0.49	1.24	0.65
Ag	0.09	0.17	0.08	0.09	0.06	1.16	0.83	0.98	1.12	0.46
Cd	0.44	1.14	0.40	0.39	0.35	0.77	1.43	1.01	0.77	0.90
Sn	2.33	1.09	1.10	1.25	1.03	1.40	1.60	1.19	1.71	1.70
Sb	132.50	125.60	32.66	60.10	29.31	11.86	35.39	26.90	44.45	638.60
Cs	0.55	2.22	0.57	0.73	0.74	2.23	4.00	3.56	1.85	2.90
Ba	27.92	1670.00	61.86	49.33	70.10	1186.00	154.40	1466.00	1400.00	1609.00
La	21.51	59.99	28.61	35.10	17.11	23.35	36.78	14.84	37.11	17.02
Ce	41.25	101.30	51.45	63.35	32.10	41.48	65.29	27.78	61.85	32.34
Pr	3.95	10.40	5.14	6.08	3.25	4.42	7.01	2.98	6.43	3.52
Nd	12.24	31.03	15.73	17.99	10.02	15.69	23.66	10.91	22.22	12.53
Sm	2.04	3.52	2.55	2.99	1.91	2.73	3.73	2.09	3.47	2.33
Eu	0.19	1.23	0.25	0.26	0.19	0.80	0.79	0.71	0.94	0.77
Gd	1.80	2.70	2.21	2.70	1.88	2.58	3.64	2.35	3.18	2.50
Tb	0.27	0.30	0.33	0.39	0.31	0.37	0.51	0.39	0.45	0.39
Dy	1.64	1.48	2.06	2.20	1.90	2.20	3.25	2.52	2.65	2.36
Ho	0.35	0.30	0.46	0.50	0.42	0.48	0.73	0.57	0.54	0.50
Er	1.11	0.89	1.44	1.57	1.33	1.46	2.31	1.73	1.56	1.50
Tm	0.18	0.14	0.25	0.26	0.23	0.24	0.36	0.27	0.25	0.23
Yb	1.32	0.98	1.75	1.85	1.59	1.66	2.43	1.82	1.57	1.51
Lu	0.21	0.16	0.29	0.31	0.27	0.28	0.39	0.29	0.25	0.23
Hf	3.94	6.29	3.87	3.67	3.48	4.30	7.83	6.02	4.54	4.82
Ta	1.27	0.37	1.17	1.22	1.05	0.32	0.54	0.42	0.33	0.40
W	31.53	29.66	28.61	30.77	22.49	21.76	15.94	18.53	15.19	93.29
Tl	0.20	1.12	0.22	0.19	0.23	1.45	1.01	2.35	1.71	1.68
Pb	5.03	23.05	2.62	5.55	3.04	277.10	59.12	17.47	37.36	15.90
Bi	0.20	0.52	0.15	0.20	0.10	0.14	0.09	0.07	0.12	0.08
Th	23.37	16.39	34.20	28.95	27.73	8.32	12.60	9.97	7.68	8.21
U	1.98	4.34	2.07	3.76	2.25	1.78	2.76	2.37	1.57	1.61
ΣREEs	88.06	214.41	112.52	135.54	72.50	97.74	150.88	69.27	142.46	77.72
ΣLREEs	81.17	207.47	103.73	125.77	64.58	88.47	137.26	59.31	132.02	68.51
ΣHREEs	6.89	6.94	8.79	9.77	7.92	9.27	13.62	9.96	10.44	9.22
$(La/Yb)_N$	11.71	43.94	11.71	13.59	7.70	10.08	10.87	5.85	16.94	8.11
Eu/Eu*	0.30	1.23	0.32	0.28	0.31	0.92	0.66	0.99	0.87	0.98
T_{Zr}(°C)	647.73	761.73	666.20	630.77	658.52	753.40	889.96	748.40	698.63	767.19

* LOI=loss on ignition; FeO^T = FeO + Fe_2O_3 * 0.8998; $Mg^\#$ = 100 × molar MgO/(MgO + FeO^T); A/CNK = molar Al_2O_3/(CaO + Na_2O + K_2O); A/NK = molar Al_2O_3/(Na_2O + K_2O); ($La/Yb)_N$ = (La_{Sample}/La_{CI})/(Yb_{Sample}/Yb_{CI}); Eu/Eu* = (Eu_{Sample}/Eu_{CI})/{[(Sm_{Sample}/Sm_{CI}) * (Gd_{Sample}/Gd_{CI})]^ (1/2)}; T_{Zr}(°C)(zirconium saturation temperature) is calculated by [44]. Normalization values are from [43].

4.2.2. Quartz Porphyry (QP)

The QP shows high SiO_2 (65.86–74.32 wt%) and K_2O (2.66–7.56 wt%) contents, but low Na_2O (0.12–0.29 wt%), FeO^T (4.82–5.53 wt%), MnO (0.16–0.28 wt%), TiO_2 (0.39–0.81 wt%) and P_2O_5 (0.12–0.20 wt%) contents and $Mg^\#$ (21.25–38.92). The value of A/CNK ranges from 1.01 to 3.36 (Figure 4d). All of the above suggested the QP was high-K subalkaline peraluminous rock. It is enriched in LREEs with $(La/Yb)_N$ of 5.85–16.94 (Figure 5c) and LILEs (Figure 5d). It also shows weakly negative Eu anomalies (0.90–0.970) (Figure 5c) and depletes in Nb, Sr, P. Ti (Figure 5d).

4.3. In Situ Zircon Hf Isotope

The data is presented in Table 3. All the $^{176}Lu/^{177}Hf$ ratios were less than 0.002, which indicated that the decay of ^{177}Hf by ^{176}Lu was rare, so the measured $^{176}Hf/^{177}Hf$ ratios likely represent the initial composition of the magmatic system [45,46]. The initial $^{176}Hf/^{177}Hf$ ratios of MG (18XSG1) and QP (18XSG2), which were calculated back to 254 Ma, ranged from 0.282576 to 0.282693 and 0.282495 to

 doi:10.20944/preprints202502.1347.v1

0.282665, respectively. Additionally, the value of $\varepsilon_{Hf}(t)$ ranges from −1.6 to 2.6 and −4.4 to 1.5, respectively (Figure 6). The two-stage model age (T_{DM2}) yielded from 1003 to 1301Ma and 947 to 1161Ma, respectively.

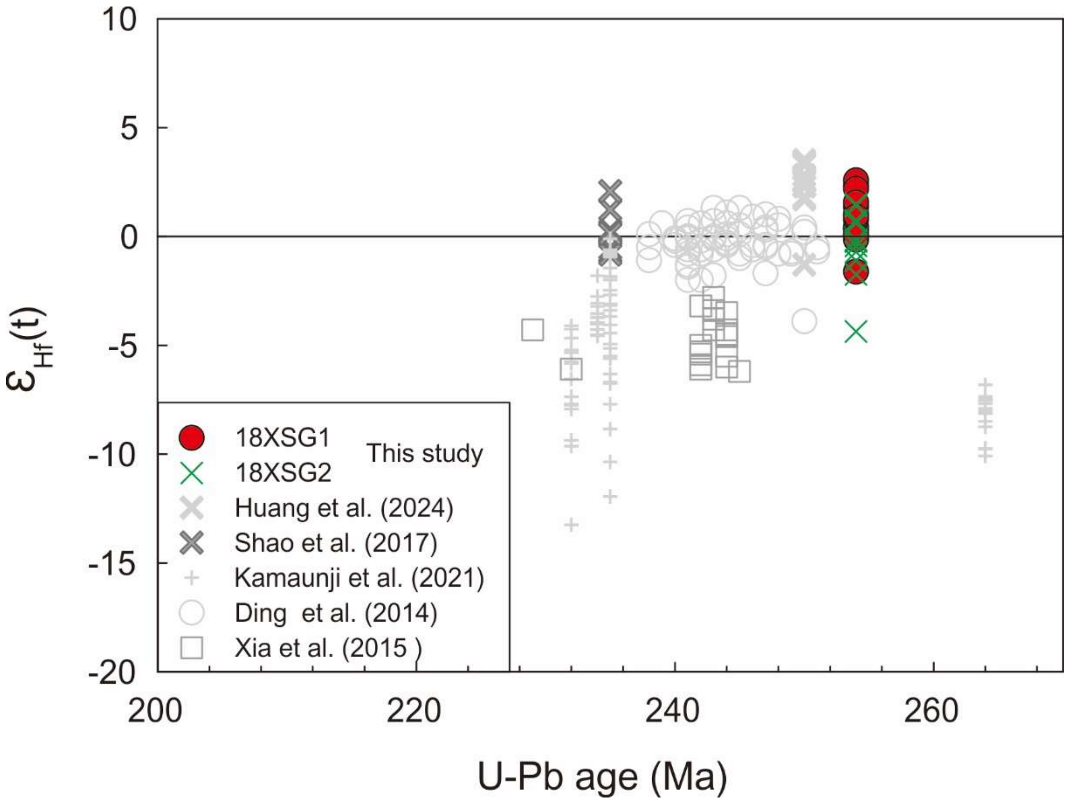

Figure 6. Diagrams of ε_{Hf} (t) vs. U-Pb age. The published zircon Hf isotopic data of granites in the EKOB is present in Supplementary Table S1.

Table 3. Zircon in-situ Lu-Hf isotopic data for Xingshugou monzogranite (18XSG1) and quartz porphyry (18XSG2).

Sample name	t (Ma)	$^{176}Yb/^{177}Hf$	2σ	$^{176}Lu/^{177}Hf$	2σ	$^{176}Hf/^{177}Hf$	2σ	$\varepsilon_{Hf}(0)$	$\varepsilon_{Hf}(t)$	2σ	T_{DM1}	T_{DM2}	$f_{Lu/Hf}$
18XSG1-monzogranite													
18XSG11-1	254	0.034836	0.000313	0.001295	0.000010	0.282638	0.000018	-4.7	0.6	0.6	876	1238	-0.96
18XSG11-2	254	0.050784	0.001333	0.001922	0.000038	0.282665	0.000020	-3.8	1.5	0.7	853	1186	-0.94
18XSG11-3	254	0.043135	0.000270	0.001606	0.000003	0.282639	0.000025	-4.7	0.6	0.9	882	1239	-0.95
18XSG11-4	254	0.065785	0.000262	0.002489	0.000020	0.282606	0.000018	-5.9	-0.7	0.6	952	1324	-0.93
18XSG11-5	254	0.041405	0.000424	0.001573	0.000009	0.282617	0.000017	-5.5	-0.2	0.6	913	1290	-0.95
18XSG11-6	254	0.029869	0.000413	0.001132	0.000018	0.282660	0.000018	-4.0	1.4	0.6	842	1189	-0.97
18XSG11-7	254	0.038559	0.000794	0.001436	0.000019	0.282590	0.000016	-6.4	-1.1	0.6	948	1349	-0.96
18XSG11-8	254	0.039654	0.000854	0.001438	0.000041	0.282615	0.000026	-5.6	-0.2	0.9	912	1292	-0.96
18XSG11-9	254	0.046882	0.000158	0.001802	0.000017	0.282618	0.000018	-5.4	-0.2	0.6	917	1289	-0.95
18XSG11-10	254	0.039331	0.000520	0.001508	0.000024	0.282616	0.000018	-5.5	-0.2	0.6	913	1292	-0.95
18XSG11-11	254	0.043702	0.001075	0.001638	0.000054	0.282498	0.000017	-9.7	-4.4	0.6	1084	1556	-0.95
18XSG11-12	254	0.043832	0.000219	0.001601	0.000015	0.282573	0.000023	-7.1	-1.7	0.8	977	1389	-0.95
18XSG11-13	254	0.050955	0.000358	0.001969	0.000009	0.282617	0.000019	-5.5	-0.2	0.7	922	1293	-0.94
18XSG11-14	254	0.038604	0.000614	0.001469	0.000029	0.282609	0.000017	-5.8	-0.4	0.6	922	1306	-0.96
18XSG11-15	254	0.033969	0.000432	0.001268	0.000020	0.282641	0.000016	-4.6	0.7	0.6	872	1233	-0.96
18XSG2-quartz porphyry													
18XSG21-1	254	0.035607	0.000158	0.001366	0.000014	0.282686	0.000022	-3.0	2.3	0.8	809	1132	-0.96
18XSG21-2	254	0.036748	0.000397	0.001443	0.000010	0.282630	0.000025	-5.0	0.3	0.9	892	1260	-0.96
18XSG21-3	254	0.033863	0.000710	0.001309	0.000020	0.282693	0.000022	-2.8	2.6	0.8	798	1116	-0.96
18XSG21-4	254	0.037836	0.000151	0.001444	0.000006	0.282623	0.000026	-5.3	0.1	0.9	902	1275	-0.96
18XSG21-5	254	0.046779	0.000269	0.001818	0.000006	0.282652	0.000019	-4.3	1.0	0.7	869	1214	-0.95
18XSG21-6	254	0.039969	0.000349	0.001492	0.000011	0.282631	0.000023	-5.0	0.4	0.8	891	1256	-0.96
18XSG21-7	254	0.040807	0.000935	0.001567	0.000027	0.282634	0.000021	-4.9	0.4	0.7	888	1251	-0.95
18XSG21-8	254	0.038238	0.000165	0.001481	0.000013	0.282660	0.000029	-4.0	1.4	1.0	850	1192	-0.96
18XSG21-9	254	0.032690	0.000530	0.001213	0.000012	0.282682	0.000022	-3.2	2.2	0.8	812	1140	-0.96

 doi:10.20944/preprints202502.1347.v1

18XSG21-10	254	0.043326	0.000585	0.001721	0.000033	0.282618	0.000029	-5.4	-0.2	1.0	915	1289	-0.95
18XSG21-11	254	0.041520	0.000398	0.001574	0.000013	0.282644	0.000025	-4.5	0.8	0.9	875	1230	-0.95
18XSG21-12	254	0.036700	0.000303	0.001430	0.000014	0.282665	0.000025	-3.8	1.6	0.9	841	1180	-0.96
18XSG21-13	254	0.032437	0.000125	0.001222	0.000003	0.282646	0.000025	-4.5	0.9	0.9	863	1221	-0.96
18XSG21-14	254	0.040993	0.001448	0.001493	0.000048	0.282623	0.000024	-5.3	0.0	0.8	903	1276	-0.96
18XSG21-15	254	0.042193	0.000783	0.001620	0.000032	0.282576	0.000025	-6.9	-1.6	0.9	973	1382	-0.95

* The parameter used in our calculations: $(^{176}Lu/^{177}Hf)_{CHUR}$ = 0.0332, $(^{176}Hf/^{177}Hf)_{CHUR}$ = 0.282772 [47]; $(^{176}Lu/^{177}Hf)_{DM}$ = 0.0384, $(^{176}Hf/^{177}Hf)_{DM}$ = 0.28325 [48]; $\lambda(^{176}Lu) = 1.867\times10^{-11}$ $^{a-1}$ [49]. The $^{176}Lu/^{177}Hf$ (*C*) = 0.015 [48]. t = 254Ma.

5. Discussion

5.1. Petrogenesis of the XSG Granitoids

I-, S-, M- and A-type granite have been presented according to the different source and geochemical characteristics [50,51]. While I- S-, and A- granites have been documented in the EKOB [3,18,19,26,52], our integrated analyses constrain the petrogenetic affinity of the XSG intrusions.

The absence of alkaline dark minerals in both MG and QP, coupled with depletion in HFSEs (Figure 5b, d), low zircon saturation temperature (T_{Zr} = 694–800 ℃ for MG, 752–880 ℃ for QP) [44,53], as well as subdued value of 10000Ga/Al ratios (1.21–1.93) and Zr + Nb + Ce + Y contents (113.11–286.50 ppm) below typical A-type granite (Figure 7e, f, g, h), collectively preclude an A-type affinity [50]. Furthermore, the scarcity of voluminous coeval mafic intrusions in the study area [31], absence of aluminum minerals (e.g., muscovite, garnet and cordierite) and negative relationship between P_2O_5 and SiO_2 in samples (Figure 7d) confirm an I-type granite classification [51,54,55].

The MG shows high SiO_2 contents (73.00–79.56 wt%) but low TiO_2 (0.08–0.21 wt%), MgO (0.11–0.24 wt%), FeO^T (1.01–1.76 wt%), P_2O_5 (0.01–0.05 wt%) and MnO (0.02–0.06 wt%) contents (Figure 7a, b, c), as well as depletes in Eu (Eu/Eu* = 0.28–0.32, one outlier at 1.23), Ba, and Sr (Figure 5a, b). The MG shows higher value of FeO^T/MgO ratios (7.20–12.36) and (K_2O + Na_2O)/CaO ratios (2.64–18.50) than QP (2.83–6.67, 1.72–3.94, respectively), and it plots into FG (fractionated granites) area in the diagrams of FeO^T/MgO vs. Zr + Nb + Ce + Y and (K_2O + Na_2O)/CaO vs. Zr + Nb + Ce + Y (Figure 7e, f). All of the above indicate the MG underwent higher degree fractional crystallization than QP. The samples of MG show significantly fractional crystallization of K-feldspar and plagioclase on the Ba/Sr–Sr and Ba–Sr diagrams (Figure 8a, b) coupled with the highly depleted Eu for MG (Figure 5a). The Rb/Sr ratios of MG are positively correlated with Sr (Figure 8c), which implies that the fractional crystallization of biotite. The $(La/Yb)_N$–La diagram shows significant fractional crystallization of titanite and apatite for MG (Figure 8d). These features collectively support the classification of the MG as metaluminous to weakly peraluminous low K calc-alkaline I-type granite that underwent extensive fractional crystallization (Figure 4b,c, d, 7, 8), contrasting with the less differentiated high K calc-alkaline I-type QP (Figure 4b,c,d, 7, 8) [51,56].

 doi:10.20944/preprints202502.1347.v1

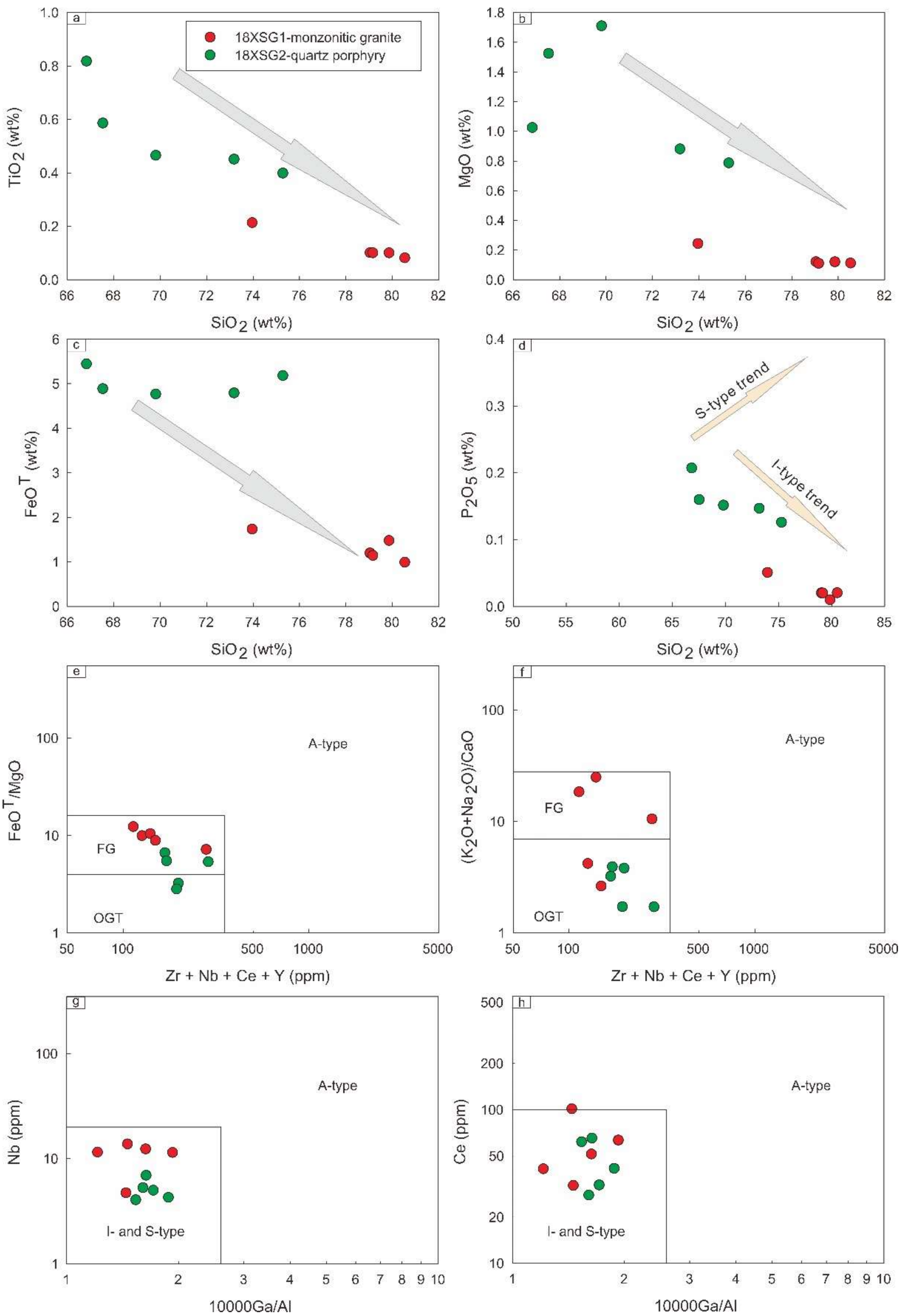

Figure 7. Diagrams of (a) TiO_2 (wt%) vs. SiO_2 (wt%); (b) MgO (wt%) vs. SiO_2 (wt%); (c) FeO^T (wt%) vs. SiO_2 (wt%); (d) P_2O_5 (wt%) vs. SiO_2 (wt%); (e) FeO^T/MgO vs. Zr + Nb + Ce + Y (ppm); (f) (K_2O + Na_2O)/CaO vs. Zr + Nb + Ce + Y (ppm); (g) Nb (ppm) vs. 10000Ga/Al; (h) Ce (ppm) vs. 10000Ga/Al. e–h are from [50]. FT = fractionated granites, OGT = unfractionated granites.

Preprints.org (www.preprints.org) | NOT PEER-REVIEWED | Posted: 18 February 2025 doi:10.20944/preprints202502.1347.v1

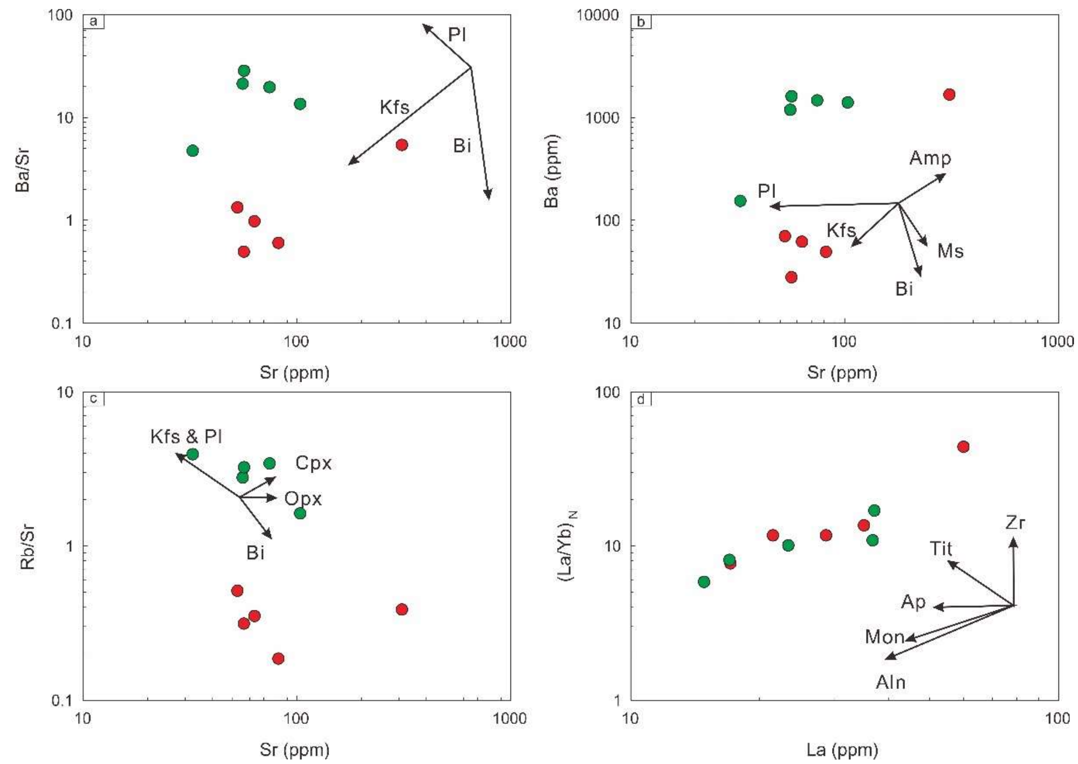

Figure 8. Diagrams of (a) Ba/Sr vs. Sr (ppm); (b) Ba (ppm) vs. Sr (ppm); (c) Rb/Sr vs. Sr (ppm); (d) $(La/Yb)_N$ vs. La (ppm). Pl = plagioclase; Kfs = K-feldspar; Bi = biotite; Amp = amphibole; Ms = muscovite; Cpx = clinopyroxene; Opx = orthopyroxene; Aln = allanite; Mon = monazite; Ap = apatite; Tit = titanite; Zr = zircon.

I-type granite genesis typically involves three principal mechanisms: (1) mixing of crustal and mantle-derived melts [57,58], (2) Assimilation fractional crystallization (AFC) of mantle-derived basaltic magma during ascent through continental crust [49,59], (3) partial melting of the lower crust [60–63].

Absence of mafic microgranular enclaves (MMEs) in MG and QP (Figure 2) and restricted zircon $\varepsilon_{Hf}(t)$ value (−1.6 to 2.6 for MG, −4.4 to 1.5 for QP) (Figure 6), precluded the magma mixing as a viable mechanism, because such a process would produce scattered isotopic signatures ($\Delta\varepsilon$ > 10 units) [61,64].

The high SiO_2 contents (exceeding 55 wt%) and low concentrations of compatible elements contents, such as Cr (3.91–6.65 ppm for MG, 4.71–7.70 ppm for QP), Ni (1.32–3.13 ppm for MG, 2.77–4.98 ppm for QP), and Co (2.25–4.01ppm for MG, 7.46–87.14 ppm for QP), suggested they couldn't generate from the mantle [65]. According to the relative incompatibility of Nb, Th, Ta and U ($D_{Nb} \approx D_{Th} < D_{Ta} \approx D_U$), Nb^* (= $[Nb/Th]_{Sample}/[Nb/Th]_{PM}$) and Ta^* (= $[Ta/U]_{Sample}/[Ta/U]_{PM}$) ratios are normally inherited from the source region and remain constant during the subsequent differentiation [66]. The lower Nb^* and Ta^* ratios compared to those of the Bulk Continental Crust (BCC) (Figure 9a) further suggest that they were not derived from the mantle. To produce one piece of granites needs more than three times of basaltic magma [49], but we haven't found so much coeval mafic magma in EKOB [25,67,68]. Consequently, we have ruled out the mechanism involving the fractionation of mantle-derived magma.

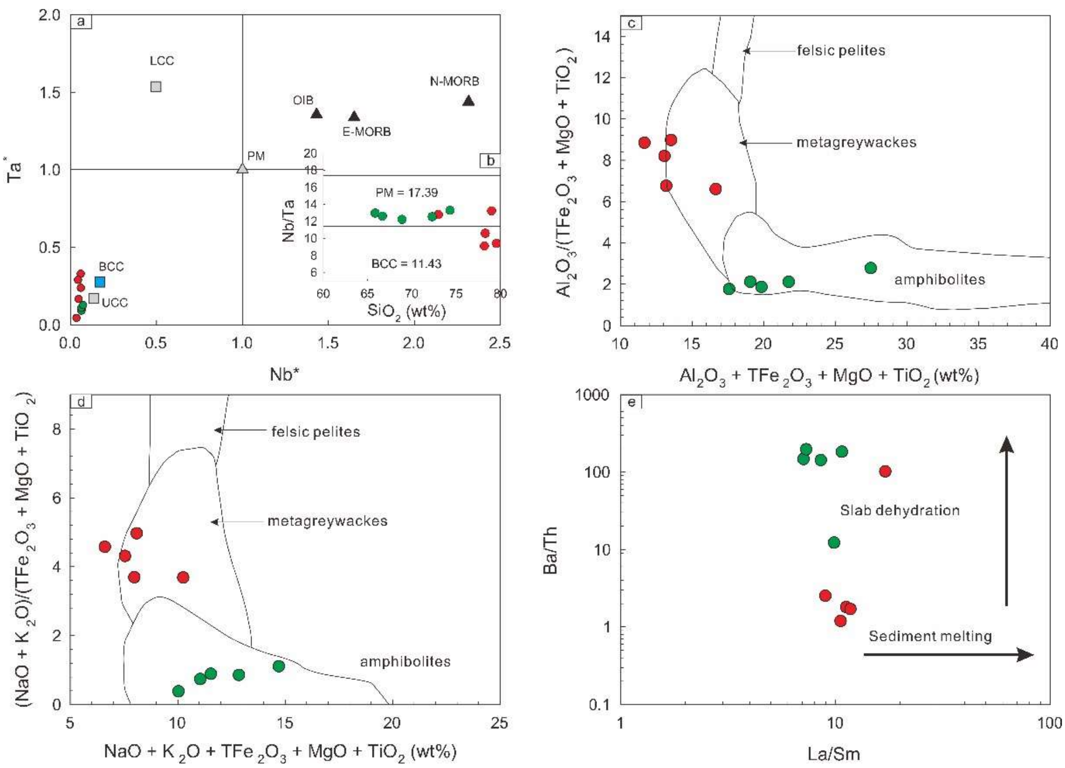

Figure 9. Diagrams of magmatic source discrimination. (a) Nb* vs. Ta* [66]; (b)SiO_2 vs. Nb/Ta; (c) Al_2O_3/(Fe_2O_3 + MgO + TiO_2) vs. Al_2O_3 + Fe_2O_3 + MgO + TiO_2 (wt%) [69,70]; (d) (Na_2O + K_2O)/(Fe_2O_3 + MgO + TiO_2) vs. Na_2O + K_2O + Fe_2O_3 + MgO + TiO_2 (wt%) [69,70]; (e) La/Sm vs. Ba/Th [71]. Data of primitive mantle and average oceanic basalts (OIB, E-MORB, N-MORB) are from [43], crust composition (BCC, LCC, UCC) are from [72]. Nb* (= $[Nb/Th]_{Sample}/[Nb/Th]_{PM}$) and Ta* (= $[Ta/U]_{Sample}/[Ta/U]_{PM}$).

The Nb/Ta ratios of the MG and QP samples range from 9.10 to 13.23 and 12.23 to 13.39, respectively (Figure 9b). These ratios cluster near BCC values (11.43), deviating markedly from primitive mantle (PM) values (17.5), indicating a crustal affinity (Figure 9b) [43,72,73]. The MG exhibits high (Na_2O + K_2O)/(Fe_2O_3 + MgO + TiO_2) and Al_2O_3/(Fe_2O_3 + MgO + TiO_2) ratios, whereas the QP shows low ratios of these parameters (Figure 9c, d). We believe that the MG also should be plotted into the amphibolites area (Figure 9c, d), as it has undergone some degree of fractional crystallization, leading to a decrease in Fe, Mg, and Ti contents. Therefore, we propose that the MG and QP are derived from mafic lower crust [69,70]. The ε_{Hf}(t) values are mostly positive (Figure 6), which indicating a mantle component. The two-stage Hf model ages of the MG and QP range from 1.0 to 1.3 Ga and 0.9 to 1.1 Ga, respectively. The MG and QP display higher Ba/Th ratios but lower La/Sm ratios (Figure 9e), which implied the source was modified by fluids released from subducted slab. The intense interaction of mantle-crustal magma has been enhanced, as evidenced by the widespread coeval MMEs during Late Permian-Middle Triassic [18,27,33].

In summary, we propose that the MG and QP originated from the partial melting of the metasomatized Meso- to Neo-Proterozoic juvenile lower crust. This process was triggered by the underplating of mantle-derived mafic magma at the boundary between the lithospheric mantle and the lower crust. Additionally, fractional crystallization occurred in the MG during magmatic evolution.

5.2. Geochronology and Tectonic Implications

Zircon U-Pb geochronology constraints the crystallization ages of the MG and QP to 254.7 ± 1.1 Ma (MSWD = 0.26, Figure 3b) and 254.3 ± 1.1 Ma (MSWD = 0.116, Figure 3e), respectively, with magmatic origins confirmed by well-developed oscillatory zoning textures (Figure 3c, f) and elevated Th/U ratios (0.28 to 5.39, Table 1) [39]. These Late Permian granitoids record critical magmatic activity during the Paleo-Tethyan evolution of the EKOB, displaying diagnostic arc-related geochemical

Preprints.org (www.preprints.org) | NOT PEER-REVIEWED | Posted: 18 February 2025 doi:10.20944/preprints202502.1347.v1

signatures including LILEs enrichment, HFSEs depletion (Figure 5), and systematic clustering within the volcanic arc granite (VAG) field on the tectonic discrimination diagrams (e.g., Nb vs. Y and Ta vs. Yb, Figure 10) [74]. Their coherent spatial-temporal distribution and subduction-related geochemical fingerprints collectively affirm generation in an active continental margin setting associated with northward Paleo-Tethyan oceanic slab subduction.

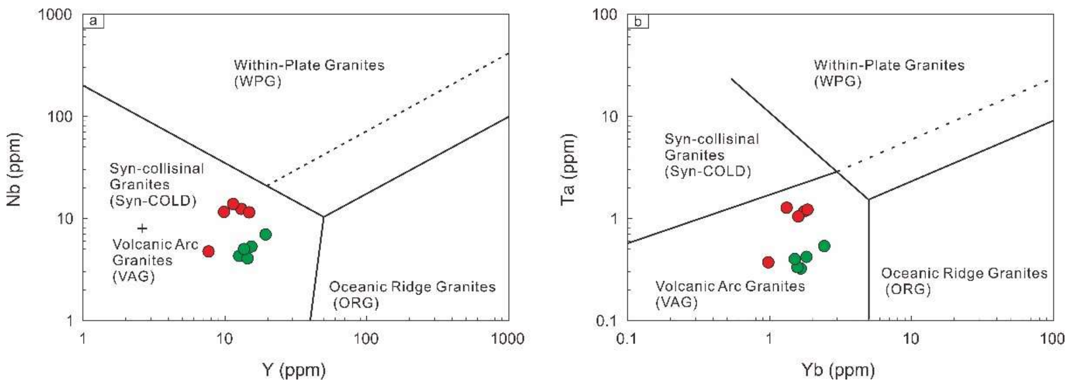

Figure 10. Diagrams of granite tectonic discrimination [74].

The tectonic evolution of the Buqingshan-A'nyemaqing Ocean (BAO), a Paleo-Tethys branch, has been progressively constrained though decades of multidisciplinary research. Current consensus recognizes oceanic opening prior to the Early Carboniferous, evidenced by ophiolitic suites including Haerguole gabbro (ca. 332 Ma [13]) and Dur'ngoi basalts (ca. 308 Ma [11]; ca. 345 Ma [12]). Northeastward subduction initiation at ca. 278 Ma is well-documented by the Xiaomiao mafic dike swarm [14], yet persistent controversies surround the timing and mechanisms of subduction-to-collision transition. Three principal models have emerged: (1) A dominant view advocates continuous subduction until ca. 240 Ma followed by Lake Triassic collision (240 Ma to 225 Ma) and post-collisional stage [2,17,32,75]. (2) Alternative interpretations propose prolonged subduction through the Late Triassic with Jurassic collision onset [20–22,76]. (3) Contrasting models posit pre-Late Permian collision [18,19,23,77]. These discrepancies stem from two key factors: methodological limitations in tectonic discrimination using granitoid geochemistry alone [26,31,67,78–80], compounded by evolving interpretations of expanding geochemical and geological datasets [8–10,30,81–83]. To reconcile these conflicts, we propose an integrated geodynamic model synthesizing stratigraphic records, petrogenetic constraints, metallogenic patterns, and regional tectonics, augmented by recent high-resolution geochronological and isotopic datasets.

The first stage (345–278 Ma): The tectonic evolution of the BAO initiated with oceanic opening prior to ca. 345 Ma, as evidenced by Haerguole and Dur'ngoi ophiolites [12], while Carboniferous shallow-marine sequences dominated by volcanic-carbonate strata reflect passive continental margin [84] without arc-magmatism (Figure 11).

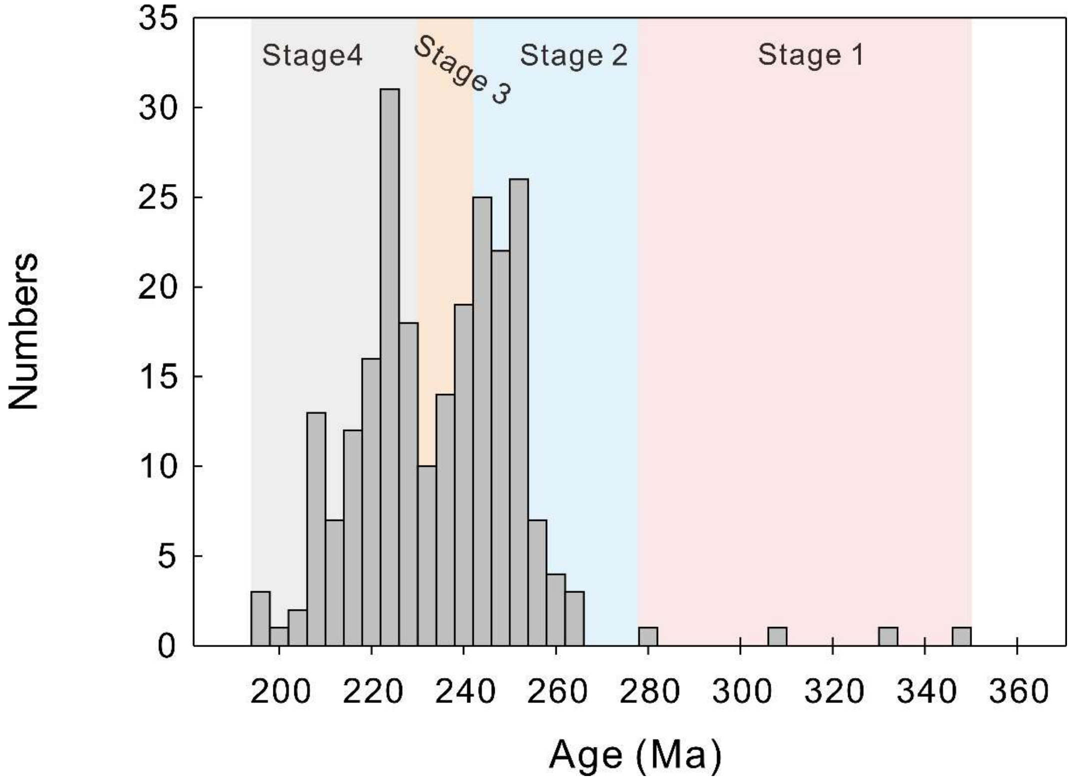

Figure 11. Histograms of zircon U-Pb ages of the Carboniferous-Triassic magmatic rocks in the EKOB. Published ages are presented in Supplementary Table S2.

The second stage (278–240 Ma): Northward subduction commenced by ca. 278 Ma, marked by the Xiaomiao mafic dike swarm [14] and corroborated by the angular unconformity between the Upper Permian Gequ Formation and underlying units [84]. The Upper Permian Gequ Formation, Lower Triassic Hongshuichuan Formation, and Middle Triassic Naocangjiangou Formation record progressive subduction [85], transitioning from low-angle slab (278–263 Ma) with limited magmatism to intense mantle-crust interaction during 263-240 Ma (Figure 11). This magmatic flare-up, characterized by diverse magmatic rocks such as I-/A_2-type granite, adakitic, and mafic rocks (Yingzhuagou olivine gabbro-norite: 263 ± 4Ma [86]; Zhongzaohuo pyroxenite: 261.2 ± 3.0 Ma [87]; Bairiqiligou mafic dike swarms: 251 ± 2 Ma [88]; Kengdenongshe granite porphyry: 257.0 ± 2.0 Ma [52]) coincided with the asthenospheric upwelling indued by the slab rollback. Mantle sources varied from enriched [68,87] to hybrid depleted-enriched compositions [86], while crustal melts derived from lower crust [89], juvenile mafic lower crust [90], and subducted slab and overlying sediments [18]. Concurrent Cu-Ni mineralized mafic-ultramafic complexes (263–252 Ma) [86–88] further attest to this extensional regime, where rollback-driven lithospheric thinning facilitated large-scale magma generation and crustal recycling through mantle-crust hybridization (Figure 11).

The Third stage (240–230 Ma): The incipient collision phase is evidenced by a micro-angular unconformity between middle Triassic Xilikete Formation and Naocangjiangou Formation, signaling initial collision between Bayanhar block and EKOB [84]. Although slab break-off has been invoked by some studies in the EKOB [91], the conspicuous magmatic quiescence during this interval (Figure 11) provides stronger evidence for syn-collisional compressional tectonics, as evidenced by localized Xilikete Formation deposition in uplifted terranes [84].

The fourth stage (230–195 Ma): The pronounced angular unconformity between the Upper Triassic Babaoshan Formation and underlying strata reflects large-scale collision during this period [84]. Geophysical constraints reveal lower crustal thinning [92,93], attributed to eclogitization-drived lithospheric delamination that triggered asthenospheric upwelling and renewed magmatic flare-up (Figure 11). This stage generated voluminous A_2-type and adakitic magma [19,26,75,79,80,94–96], their emplacement facilitated by gravitational instability of densified lithospheric roots.

 doi:10.20944/preprints202502.1347.v1

Synthesizing multidisciplinary evidence, we reconstruct the BAO evolutionary sequence: (1) The BAO has opened before early Carboniferous (ca. 345 Ma); (2) the oceanic slab has initiated to subduct before 278 Ma; (3) then it evolved into the low-angle subduction during 278–263 Ma and high-angle subduction caused by slab roll-back during 263–240 Ma; (4) the EKOB and Bayanhar has collided together during 240–230 Ma; (5) finally, the EKOB has evolved into the post-collisional setting during 230–195 Ma.

6. Conclusions

(1) Zircon U-Pb geochronology constrains the emplacement of monzogranite and quartz porphyry to ca. 254 Ma, classifying as low-K calc-alkaline I-type granites which underwent highly fractional crystallization, and high-K calc-alkaline I-type granites, respectively.

(2) Petrogenetic modeling indicates these granitoids originated through partial melting of juvenile mafic lower crust, a process initiated by mantle-derived magma underplating.

(3) The integrated geodynamic evolution of Buqingshan-A'nyemaqing ocean (a branch of Paleo-Tethys Ocean) has been established as follows: (1) oceanic spreading initiates before ca. 345 Ma, (2) low-angle subduction stage ranges from ca. 278 to 263 Ma, (3) slab roll-back stage ranges from ca. 263 to 240 Ma, (4) syn-collisional stage ranges from ca. 240 to 230 Ma, (5) post-collisional stage ranges from 230 to 195 Ma.

Supplementary Materials: The following supporting information can be downloaded at the website of this paper posted on Preprints.org. Table S1: Summary of the published zircon Hf isotopic data of granites in the EKOB. Table S2: Summary of ages of the Permian-Triassic igneous rocks in the eastern of the East Kunlun Orogenic Belt.

Author Contributions: Conceptualization, Chao Hui and Fengyue Sun; Formal analysis, Tao Yu; Funding acquisition, Tao Wang, Yanqian Yang and Yun Chai; Investigation, Yanqian Yang, Bile Li, Xingsen Chen, Chengxian Liu and Xinran Zhu; Methodology, Chao Hui; Project administration, Desheng Dou; Software, Bakht Shahzas; Supervision, Fengyue Sun; Validation, Jiaming Yan; Visualization, Yajing Zhang, Yuxiang Wang, Zhengsong Wang, Hanran Li and Renyi Song; Writing – original draft, Chao Hui; Writing – review & editing, Fengyue Sun. All authors have read and agreed to the published version of the manuscript.

Funding: This research was funded by Qinghai Geological Survey Project and Technology Innovation Center for Exploration and Exploitation of Strategic Mineral Resources in Plateau Desert Region, Ministry of Natural Resources Project, grant number 2021074005ky005, 2023085029ky004, No. 2022012005ky005, No. 2023085026ky001.

Data Availability Statement: The original contributions presented in the study are included in the article/Supplementary Material.

Acknowledgments: We would like to thank Electron Microscope Center, Jilin University, the Key Laboratory of Mineral Resources Evaluation in Northeast Asia, Ministry of Natural Resources of China, Jilin University, Langfang Tuoxuan Rock and Mineral Testing Service Co., Ltd., for helping in the analyses. We thank all the editors and anonymous reviewers for their constructive comments to improve this manuscript.

Conflicts of Interest: The authors declare no conflicts of interest.

Abbreviations

The following abbreviations are used in this manuscript:

EKOB	East Kunlun Orogenic Belt
BAO	Buqingshan-A'nyemaqing Ocean
AOB	A'nyemaqen ophiolitic belt
NKB	Caledonian back-arc basin of Northern East Kunlun Orogenic Belt
CKB	uplifted granitic basement of Central East Kunlun Orogenic Belt
SKB	composite accretion of the Southern East Kunlun Orogenic Belt

NEKF	northern east Kunlun fault
CEKF	central east Kunlun fault
SEKF	southern east Kunlun fault
ATF	Altyn Tagh strike-slip fault
MMF	Wenquangou-Wahongshan fault
XSG	Xingshugou
MG	Monzogranite
Qtz	quartz
Pl	plagioclase
Kfs	potassium feldspar
QP	Quartz porphyry
CL	cathodoluminescence
LREEs	light rare earth elements
T_{DM2}	two-stage model age

References

1. Bian, Q.-T.; Li, D.-H.; Pospelov, I.; Yin, L.-M.; Li, H.-S.; Zhao, D.-S.; Chang, C.-F.; Luo, X.-Q.; Gao, S.-L.; Astrakhantsev, O.; et al. Age, geochemistry and tectonic setting of Buqingshan ophiolites, North Qinghai-Tibet Plateau, China. *Journal of Asian Earth Sciences* **2004**, *23*, 577-596, doi:10.1016/j.jseaes.2003.09.003.
2. Dong, Y.; He, D.; Sun, S.; Liu, X.; Zhou, X.; Zhang, F.; Yang, Z.; Cheng, B.; Zhao, G.; Li, J. Subduction and accretionary tectonics of the East Kunlun orogen, western segment of the Central China Orogenic System. *Earth-Science Reviews* **2018**, *186*, 231-261, doi:10.1016/j.earscirev.2017.12.006.
3. Li, R.; Pei, X.; Pei, L.; Li, Z.; Chen, G.; Chen, Y.; Liu, C.; Wang, M. The Early Triassic Andean-type Halagatu granitoids pluton in the East Kunlun orogen, northern Tibet Plateau: Response to the northward subduction of the Paleo-Tethys Ocean. *Gondwana Research* **2018**, *62*, 212-226, doi:10.1016/j.gr.2018.03.005.
4. Li, Z.-C.; Pei, X.-Z.; Bons, P.D.; Li, R.-B.; Pei, L.; Chen, G.-C.; Chen, Y.-X.; Liu, C.-J.; Wang, M.; Zhao, S.-W.; et al. Petrogenesis and tectonic setting of the early-middle triassic subduction-related granite in the eastern segment of East Kunlun: evidences from petrology, geochemistry, and zircon U-Pb-Hf isotopes. *International Geology Review* **2021**, *64*, 698-721, doi:10.1080/00206814.2021.1875268.
5. Wu, D.-Q.; Sun, F.-Y.; Pan, Z.-C.; Tian, N. Geochronology, geochemistry, and Hf isotopic compositions of Triassic igneous rocks in the easternmost segment of the East Kunlun Orogenic Belt, NW China: implications for magmatism and tectonic evolution. *International Geology Review* **2020**, 1-19, doi:10.1080/00206814.2020.1740895.
6. Xue, H.-R.; Sun, F.-Y.; Li, L.; Xin, W. Geochronology, geochemistry, and Sr–Nd–Hf isotopes of the Late Permian–Early Triassic granitoids in Eastern Kunlun Orogen, Northwest China: petrogenesis and implications for geodynamic setting. *International Geology Review* **2020**, 1-21, doi:10.1080/00206814.2020.1722968.
7. Pan, Z.; Sun, F.; Cong, Z. Petrogenesis, Sources, and Tectonic Settings of Triassic Volcanic Rocks in the Ela Mountain Area of the East Kunlun Orogen: Insights from Geochronology, Geochemistry and Hf Isotopic Compositions. *Minerals* **2022**, *12*, doi:10.3390/min12091085.
8. Xu, Q.; Sun, Y.; Mao, G.; Xin, W.; Yang, Y. Petrogenesis of the Ore-Related Intrusions of the Aikengdelesite Mo (–Cu) and Halongxiuma Mo Deposits: Implication for Geodynamic Evolution and Mineralization in the East Kunlun Orogen, Northwest China. *Minerals* **2023**, *13*, doi:10.3390/min13030447.
9. Zhang, B.; Dong, Y.; Sun, S.; He, D.; Hui, B.; Yue, Y.; Ren, X.; He, W. Late Triassic extension of thickened lithosphere of the East Kunlun orogenic Belt, northern Tibetan Plateau: Evidence from the geochemistry and geochronology of mafic magmatism. *Gondwana Research* **2025**, *137*, 99-116, doi:https://doi.org/10.1016/j.gr.2024.08.018.
10. Li, H.-R.; Qiao, J.-F.; Sun, F.-Y.; Qian, Y.; Wang, Y.-Z.; Bakht, S.; Liu, H.-T.; Gu, Y. Three episodes of Triassic volcanism in the Eastern Kunlun Orogen, NW China: constraints for evolution of the Palaeo-Tethys Ocean. *International Geology Review* **2024**, *66*, 1815-1837, doi:10.1080/00206814.2023.2251547.
11. Yang, J.; Shi, R.; Wu, C.; Wang, X.; Robinson, P.T. Dur'ngoi ophiolite in East Kunlun, Northeast Tibetan plateau: Evidence for paleo-Tethyan suture in Northwest China. *Journal of Earth Science* **2009**, *20*, 303-331, doi:10.1007/s12583-009-0027-y.

12. Chen, L.; Sun, Y.; Pei, X.; Gao, M. Northernmost paleo-tethyan oceanic basin in Tibet:Geo-chronological evidence from ~(40)Ar/~(39)Ar age dating of Dur'ngoi ophiolite %J Chinese Science Bulletin. *Chinese Science Bulletin* **2001**, *46*, 1203-1205.
13. Liu, Z.Q.; Pei, X.-Z.; Liu, R.B.; Li, Z.-C.; Zhang, X.F.; Liu, Z.G.; Chen, G.-C.; Chen, Y.-X.; Ding, S.P.; Guo, J.F. LA-ICP-MS Zircon U-Pb Geochronology of the Two Suites of Ophiolites at the Buqingshan Area of the A'nyemaqen Orogenic Belt in the Southern Margin of East Kunlun and Its Tectonic Implication. *Acta GeoloGICA SINICA* **2011**, *85*, 185-194. (in Chinese with English abstract).
14. Liu, B.; Ma, C.-Q.; Zhang, J.-Y.; Xiong, F.-H.; Huang, J.; Jiang, H.-A. 40Ar–39Ar age and geochemistry of subduction-related mafic dikes in northern Tibet, China: petrogenesis and tectonic implications. *International Geology Review* **2014**, *56*, 57-73, doi:10.1080/00206814.2013.818804.
15. Pan, Z.; Sun, F.; Cong, Z.; Tian, N.; Xin, W.; Wang, L.; Zhang, Y.; Wu, D. Petrogenesis and Tectonic Implications of the Triassic Granitoids in the Ela Mountain Area of the East Kunlun Orogenic Belt. *Minerals* **2022**, *12*, doi:10.3390/min12070880.
16. Zhao, X.; Fu, L.; Wei, J.; Bagas, L.; Santosh, M.; Liu, Y.; Zhang, D.; Zhou, H. Late Permian back-arc extension of the eastern Paleo-Tethys Ocean: Evidence from the East Kunlun Orogen, Northern Tibetan Plateau. *Lithos* **2019**, *340-341*, 34-48, doi:10.1016/j.lithos.2019.05.006.
17. Xia, R.; Deng, J.; Qing, M.; Li, W.; Guo, X.; Zeng, G. Petrogenesis of ca. 240 Ma intermediate and felsic intrusions in the Nan'getan: Implications for crust–mantle interaction and geodynamic process of the East Kunlun Orogen. *Ore Geology Reviews* **2017**, *90*, 1099-1117, doi:10.1016/j.oregeorev.2017.04.002.
18. Huang, H.; Niu, Y.; Nowell, G.; Zhao, Z.; Yu, X.; Zhu, D.-C.; Mo, X.; Ding, S. Geochemical constraints on the petrogenesis of granitoids in the East Kunlun Orogenic belt, northern Tibetan Plateau: Implications for continental crust growth through syn-collisional felsic magmatism. *Chemical Geology* **2014**, *370*, 1-18, doi:10.1016/j.chemgeo.2014.01.010.
19. Kong, J.; Niu, Y.; Hu, Y.; Zhang, Y.; Shao, F. Petrogenesis of the Triassic granitoids from the East Kunlun Orogenic Belt, NW China: Implications for continental crust growth from syn-collisional to post-collisional setting. *Lithos* **2020**, *364-365*, 105513, doi:10.1016/j.lithos.2020.105513.
20. Yuan, C.; Sun, M.; Xiao, W.; Wilde, S.; Li, X.; Liu, X.; Long, X.; Xia, X.; Ye, K.; Li, J. Garnet-bearing tonalitic porphyry from East Kunlun, Northeast Tibetan Plateau: implications for adakite and magmas from the MASH Zone. *International Journal of Earth Sciences* **2009**, *98*, 1489-1510, doi:10.1007/s00531-008-0335-y.
21. Wang, Q.; Li, Z.-X.; Chung, S.-L.; Wyman, D.A.; Sun, Y.-L.; Zhao, Z.-H.; Zhu, Y.-T.; Qiu, H.-N. Late Triassic high-Mg andesite/dacite suites from northern Hohxil, North Tibet: Geochronology, geochemical characteristics, petrogenetic processes and tectonic implications. *Lithos* **2011**, *126*, 54-67, doi:10.1016/j.lithos.2011.06.002.
22. Yin, H.; Harrison. Geologic Evolution of the Himalayan-Tibetan Orogen **2000**.
23. Shao, F.; Niu, Y.; Liu, Y.; Chen, S.; Kong, J.; Duan, M. Petrogenesis of Triassic granitoids in the East Kunlun Orogenic Belt, northern Tibetan Plateau and their tectonic implications. *Lithos* **2017**, *282-283*, 33-44, doi:10.1016/j.lithos.2017.03.002.
24. Kamaunji, V.D.; Wang, L.-X.; Ma, C.-Q.; Liu, J.; Zhu, Y.-X. Petrogenesis and tectonic implication of the Permian-Triassic syenogranites from the eastern segment of the East Kunlun Orogen, China. *Lithos* **2021**, *402-403*, doi:10.1016/j.lithos.2020.105932.
25. Yao, L.; Dong, S.Y.; Lü, Z.C.; Zhao, C.S.; Pang, Z.S.; Yu, X.F.; Xue, J.L.; Geng, L.; Zhang, Z.H.; Liu, Y. Origin of the Late Permian gabbros and Middle Triassic granodiorites and their mafic microgranular enclaves from the Eastern Kunlun Orogen Belt : Implications for the subduction of the Palaeo-Tethys Ocean and continent–continent collision. *Geological Journal* **2018**, *55*, 147-172, doi:10.1002/gj.3340.
26. Ding, Q.-F.; Jiang, S.-Y.; Sun, F.-Y. Zircon U–Pb geochronology, geochemical and Sr–Nd–Hf isotopic compositions of the Triassic granite and diorite dikes from the Wulonggou mining area in the Eastern Kunlun Orogen, NW China: Petrogenesis and tectonic implications. *Lithos* **2014**, *205*, 266-283, doi:10.1016/j.lithos.2014.07.015.
27. Xia, R.; Wang, C.; Qing, M.; Li, W.; Carranza, E.J.M.; Guo, X.; Ge, L.; Zeng, G. Zircon U–Pb dating, geochemistry and Sr–Nd–Pb–Hf–O isotopes for the Nan'getan granodiorites and mafic microgranular

enclaves in the East Kunlun Orogen: Record of closure of the Paleo-Tethys. *Lithos* **2015**, *234-235*, 47-60, doi:10.1016/j.lithos.2015.07.018.
28. Yin, S.; Ma, C.; Xu, J. Geochronology, geochemical and Sr–Nd–Hf-Pb isotopic compositions of the granitoids in the Yemaquan orefield, East Kunlun orogenic belt, northern Qinghai-Tibet Plateau: Implications for magmatic fractional crystallization and sub-solidus hydrothermal alteration. *Lithos* **2017**, *294-295*, 339-355, doi:10.1016/j.lithos.2017.10.012.
29. Qu, H.; Friehauf, K.; Santosh, M.; Pei, R.; Li, D.; Liu, J.; Zhou, S.; Wang, H. Middle–Late Triassic magmatism in the Hutouya Fe–Cu–Pb–Zn deposit, East Kunlun Orogenic Belt, NW China: Implications for geodynamic setting and polymetallic mineralization. *Ore Geology Reviews* **2019**, *113*, doi:10.1016/j.oregeorev.2019.103088.
30. Yin, S.; Ma, C.; Xu, J.; Fu, J.; Zhang, X.-N. The role of crystal mush in porphyry systems: A case study from the Baishiya ore field, East Kunlun orogenic belt, northern Qinghai-Tibet plateau. *Ore Geology Reviews* **2022**, *146*, doi:10.1016/j.oregeorev.2022.104962.
31. Mo, X.X.; Luo, Z.H.; Deng, J.F.; Yu, X.H.; Liu, C.D.; CHen, H.W.; Yuan, W.M.; Liu, Y.H. Granitoids and Crustal Growth in the East-Kunlun Orogenic Belt. *Geological Journal of China Universityies* **2007**, *13*, 403-414. (in Chinese with English abstract).
32. Sun, F.Y.; Li, B.L.; Ding, Q.F.; Zhao, J.W.; Pan, T.; Yu, X.F.; Wang, L.; Chen, G.J.; Ding, Z.J. *Research on Major Prospecting Challenges in the East Kunlun Metallogenic Belt*; 2009. (in Chinese).
33. Xiong, F.; Ma, C.; Zhang, J. The origin of mafic microgranular enclaves and their host granodiorites from East Kunlun, Northern Qinghai-Tibet Plateau: implications for magma mixing during subduction of Paleo-Tethyan Lithosphere *Miner Petrol* **2012**, *104*, 211-224, doi:10.1007/s00710-011-0187-1.
34. Yuan, C.; Zhou, M.-F.; Sun, M.; Zhao, Y.; Wilde, S.; Long, X.; Yan, D. Triassic granitoids in the eastern Songpan Ganzi Fold Belt, SW China: Magmatic response to geodynamics of the deep lithosphere. *Earth and Planetary Science Letters* **2010**, *290*, 481-492, doi:https://doi.org/10.1016/j.epsl.2010.01.005.
35. Liu, Y.; Gao, S.; Hu, Z.; Gao, C.; Zong, K.; Wang, D. Continental and Oceanic Crust Recycling-induced Melt-Peridotite Interactions in the Trans-North China Orogen: U-Pb Dating, Hf Isotopes and Trace Elements in Zircons from Mantle Xenoliths. *Journal of Petrology* **2010**, *51*.
36. Liu, Y.; Hu, Z.; Gao, S.; Günther, D.; Xu, J.; Gao, C.; Chen, H. In situ analysis of major and trace elements of anhydrous minerals by LA-ICP-MS without applying an internal standard. *Chemical Geology* **2008**, *257*, 34-43, doi:https://doi.org/10.1016/j.chemgeo.2008.08.004.
37. Ludwig, K.R. User's Manual for Isoplot 3.00 - A Geochronological Toolkit for Microsoft Excel. *Berkeley Geochronology Center Special Publication* **2003**, *4*, 1-4.
38. Wu, F.-Y.; Yang, Y.-H.; Xie, L.-W.; Yang, J.-H.; Xu, P. Hf isotopic compositions of the standard zircons and baddeleyites used in U–Pb geochronology. *Chemical Geology* **2006**, *234*, 105-126, doi:https://doi.org/10.1016/j.chemgeo.2006.05.003.
39. Hoskin, P.W.O. The Composition of Zircon and Igneous and Metamorphic Petrogenesis. *Reviews in Mineralogy and Geochemistry* **2003**, *53*, 27-62, doi:10.2113/0530027.
40. Streckeisen, A.L. To each plutonic rock its proper name. Earth Sci Rev 12: 1-33. *Earth-Science Reviews* **1976**, *12*, 1-33.
41. Middlemost, E.A.K. Naming materials in the magma/igneous rock system. *Earth-Science Reviews* **1994**, *37*, 215-224, doi:https://doi.org/10.1016/0012-8252(94)90029-9.
42. Rickwood, P.C. Boundary lines within petrologic diagrams which use oxides of major and minor elements. *Lithos* **1989**, *22*, 247-263, doi:https://doi.org/10.1016/0024-4937(89)90028-5.
43. Sun, S.s.; McDonough, W.F. Chemical and isotopic systematics of oceanic basalts: implications for mantle composition and processes. *Geological Society, London, Special Publications* **1989**, *42*, 313-345, doi:10.1144/gsl.Sp.1989.042.01.19.
44. Miller, C.F.; McDowell, S.M.; Mapes, R.W. Hot and cold granites: Implications of zircon saturation temperatures and preservation of inheritance *Geology* **2003**, *31*, 529-532.
45. Peter D. Kinny, W.C.a.I.S.W. A reconnaissance ion-probe study of hafnium isotopes in zircons. *Geochimica et Cosmochimica Acta* **1991**, *55*, 849-859.

46. Wu, F.Y.; Li, X.H.; Zheng, Y.F.; Gao, S. Lu-Hf Isotopic Systematics and their Applicaitons in Petrology. *Acta Petrologica Sinica* **2007**, *23*, 185-220. (in Chinese with English abstract).
47. Blichert-Toft, J.; Chauvel, C.; Albarède, F. Separation of Hf and Lu for high-precision isotope analysis of rock samples by magnetic sector-multiple collector ICP-MS. *Contributions to Mineralogy and Petrology* **1997**, *127*, 248-260, doi:10.1007/s004100050278.
48. Griffin, W.L.; Pearson, N.J.; Belousova, E.; Jackson, S.E.; van Achterbergh, E.; O'Reilly, S.Y.; Shee, S.R. The Hf isotope composition of cratonic mantle: LAM-MC-ICPMS analysis of zircon megacrysts in kimberlites. *Geochimica et Cosmochimica Acta* **2000**, *64*, 133-147, doi:https://doi.org/10.1016/S0016-7037(99)00343-9.
49. Sisson, T.W.; Ratajeski, K.; Hankins, W.B.; Glazner, A.F. Voluminous granitic magmas from common basaltic sources. *Contributions to Mineralogy and Petrology* **2004**, *148*, 635-661, doi:10.1007/s00410-004-0632-9.
50. Whalen, J.B.; Currue, K.L.; Chappell, B.W. A-type granites: geochemical characteristics，discrimination and petrogenesis *Contributinons to Mineralogy and Petrology* **1987**, *95*, 407-419.
51. Chappell, B.W.; White, A.J.R. Two contrasting granite types: 25 years later *Australian Journal of Earth Sciences* **2001**, *48*, 489.
52. Zhao, X.; Wei, J.; Fu, L.; Huizenga, J.M.; Santosh, M.; Chen, J.; Wang, D.; Li, A. Multi-stage crustal melting from Late Permian back-arc extension through Middle Triassic continental collision to Late Triassic post-collisional extension in the East Kunlun Orogen. *Lithos* **2020**, *360-361*, doi:10.1016/j.lithos.2020.105446.
53. Boehnke, P.; Watson, E.B.; Trail, D.; Harrison, T.M.; Schmitt, A.K. Zircon saturation re-revisited. *Chemical Geology* **2013**, *351*, 324-334, doi:10.1016/j.chemgeo.2013.05.028.
54. Chappell, B.W. Aluminium saturation in I- and S-type granites and the characterization of fractionated haplogranites *LIthos* **1999**, *46*, 535-551.
55. Chappell, B.W.; White, A.J.R. I- and S-type granites in the Lachlan Fold Belt. *Earth and Environmental Science Transactions of the Royal Society of Edinburgh* **2011**, *83*, 1-26, doi:10.1017/s0263593300007720.
56. Wu, F.; Liu, X.; Ji, W.; Wan, J.; Yang, L. Highly fractionated granites: Recognition and research. *SCIENCE CHINA Earth Sciences* **2017**, *60*, 1201-1219, doi:https://doi.org/10.1007/s11430-016-5139-1.
57. Collins, W.J. Evaluation of petrogenetic models for Lachlan Fold Belt granitoids: Implications for crustal architecture and tectonic models. *Australian Journal of Earth Sciences* **1998**, *45*, 483-500, doi:10.1080/08120099808728406.
58. Gray, C.M.; Kemp, A.I.S. The two-component model for the genesis of granitic rocks in southeastern Australia — Nature of the metasedimentary-derived and basaltic end members. *Lithos* **2009**, *111*, 113-124, doi:10.1016/j.lithos.2009.04.010.
59. Clemens, J.D.; Darbyshire, D.P.F.; Flinders, J. Sources of post-orogenic calcalkaline magmas: The Arrochar and Garabal Hill–Glen Fyne complexes, Scotland. *Lithos* **2009**, *112*, 524-542, doi:10.1016/j.lithos.2009.03.026.
60. Gao, P.; Zheng, Y.F.; Zhao, Z.F. Experimental melts from crustal rocks: A lithochemical constraint on granite petrogenesis. *Lithos* **2016**, *266-267*, 133-157, doi:10.1016/j.lithos.2016.10.005.
61. Kemp, A.I.S.; Hawkesworth, C.J.; Foster, G.L.; Paterson, B.A.; Woodhead, J.D.; Hergt, J.M.; Gray, C.M.; Whitehouse, M.J. Magmatic and Crustal Differentiation History of Granitic Rocks from Hf-O Isotopes in Zircon. *Science* **2007**, *315*, 980-983.
62. Roberts, M.P.; Clemens, J.D. Origin of high-potassium, calc-alkaline I-type granitoids. *Geology* **1993**, *21*, 825-828.
63. Wu, F.-y.; Jahn, B.-m.; Wilde, S.A.; Lo, C.-H.; Yui, T.-F.; Lin, Q.; Ge, W.-c.; Sun, D.-y. Highly fractionated I-type granites in NE China (II): isotopic geochemistry and implications for crustal growth in the Phanerozoic. *Lithos* **2003**, *67*, 191-204, doi:10.1016/s0024-4937(03)00015-x.
64. Griffin, W.L.; Wang, X.; Jackson, S.E.; Pearson, N.J.; O'Reilly, S.Y.; Xu, X.; Zhou, X. Zircon chemistry and magma mixing, SE Chian: In-suit analysis of Hf isotopes, Tonglu and Pingtan igneous complexes. *Lithos* **2002**, *61*, 237-269.
65. Baker, M.B.; Hirschmann, M.M.; Ghiorso, M.S.; Stolper, E.M. Compositions of near-solidus peridotite melts from experiments and thermodynamic calculations. *Nature* **1993**, *375*, 308-311.
66. Niu, Y.; Batiza, R. Trace element evidence from seamounts for recycled oceanic crust in the Eastern Pacific mantle. *Earth and Planetary Science Letters* **1997**, *148*, 471-483, doi:10.1016/s0012-821x(97)00048-4.

67. Hu, Y.; Niu, Y.; Li, J.; Ye, L.; Kong, J.; Chen, S.; Zhang, Y.; Zhang, G. Petrogenesis and tectonic significance of the late Triassic mafic dikes and felsic volcanic rocks in the East Kunlun Orogenic Belt, Northern Tibet Plateau. *Lithos* **2016**, *245*, 205-222, doi:10.1016/j.lithos.2015.05.004.
68. Xiong, F.; Ma, C.; Chen, B.; Ducea, M.N.; Hou, M.; Ni, S. Intermediate-mafic dikes in the East Kunlun Orogen, Northern Tibetan Plateau: A window into paleo-arc magma feeding system. *Lithos* **2019**, *340-341*, 152-165, doi:10.1016/j.lithos.2019.05.012.
69. Rapp, R.P.; Watson, E.B. Dehydration Melting of Metabasalt at 8-32 kbar: Implications for Continental Growth and Crust-Mantle Recycling. *Journal of Petrology* **1995**, *36*, 891-931, doi:10.1093/petrology/36.4.891.
70. Rapp, R.P.; Watson, E.B.; Miller, C.F. Partial melting of amphibolite/eclogite and the origin of Archean trondhjemites and tonalites. *Precambrian Research* **1991**, *51*, 1-25, doi:https://doi.org/10.1016/0301-9268(91)90092-O.
71. Fu, L.; Bagas, L.; Wei, J.; Chen, Y.; Chen, J.; Zhao, X.; Zhao, Z.; Li, A.; Zhang, W. Growth of early Paleozoic continental crust linked to the Proto-Tethys subduction and continental collision in the East Kunlun Orogen, northern Tibetan Plateau. *GSA Bulletin* **2022**, doi:10.1130/b36292.1.
72. Rudnick, R.L.; Gao, S. *Composition of the continental crust. In: Holland, H. D., Turekian, K. K. (Eds), Treatise on Geochemistry 3.*; Elsevier-Pergamon: 2003.
73. Green, T.H. Significance of Nb/Ta as an indicator of geochemical processes in the crust-mantle system. *Chemical Geology* **1995**, *120*, 347-359.
74. Pearce, J.A.; Harris, N.B.W.; Tindle, A.G. Trace Element Discrimination Diagrams for the Tectonic Interpretation of Granitic Rocks. *Journal of Petrology* **1984**, *25*, 956-983, doi:10.1093/petrology/25.4.956.
75. Xiong, F.; Ma, C.; Zhang, J.; Liu, B.; Jiang, H.a. Reworking of old continental lithosphere: an important crustal evolution mechanism in orogenic belts, as evidenced by Triassic I-type granitoids in the East Kunlun orogen, Northern Tibetan Plateau. *Journal of the Geological Society* **2014**, *171*, 847-863, doi:10.1144/jgs2013-038.
76. Liu, H. Petrology, geochemistry and geochronology of late Triassic volcanics, Kunlun orogenic belt, western China: Implications for tectonic setting and petrogenesis. *Geochemical Journal* **2005**, *39*, 1-20, doi:10.2343/geochemj.39.1.
77. Wang, G.C.; Jia, C.X.; Zhu, Y.H. *Regional Geological Report of Alake Lake Map (in Chinese)*; China University of Geosciences Press: Wuhan, 2003.
78. Wu, F.Y.; Li, X.H.; Yang, J.-H.; Zheng, Y.F. Discussions on the petrogenesis of granites. *Acta Petrologica Sinica* **2007**, *23*, 1217-1238. (in Chinese with English abstract).
79. Qian, B.; Gao, Y.B.; Li, K.; Zhang, Z.W.; Zhou, A.S.; Wu, Y.S. Zircon U-Pb-Hf isotopes and whole rock geochemistry constraints on the petrogenesis of iron-rare metal mineralization related alkaline granitic intrusive rock in Yugouzi area, eastern Kunlun, Xinjiang. *Acta Petrologica Sinica* **2015**, *31*, 2508-2520. (in Chinese with English abstract).
80. Liu, Y.H.; Mo, X.X.; Yu, X.H.; Zhang, X.T.; Xu, G.W. Zirocn SHRIMP U-Pb dating of the Jingren granite, Yemaquan region of the east Kunlun and its geological signigicance. *Acta Petrologica Sinica* **2006**, *22*, 2457-2463. (in Chinese with English abstract).
81. Liu, B.; Zhou, Q.; Jarquín, E.; Sha, H.; Wang, R. Late Cretaceous-Palaeocene arc magmatism in Bumeicun, Gangdese, southern Tibet: Products of slab rollback of Neo-Tethyan Ocean? *Geological Journal* **2023**, doi:10.1002/gj.4719.
82. Zhang, J.; Chai, J.; Zhang, L.; Huang, Q.; Wang, Q.; Pan, L.; Ma, C.; Li, J.; Pan, Y. Lower crustal copper enrichment and mobilization indicated by Late Permian amphibole gabbros and granodiorites in the eastern Kunlun Orogen, northern Tibet. *Lithos* **2024**, *482-483*, 107740, doi:https://doi.org/10.1016/j.lithos.2024.107740.
83. Zhang, M.; Tan, S.; Ruan, M.; Li, L.; Yan, Q. Petrogenesis and tectonic implication of the Triassic monzogranite from the central segment of the East Kunlun Orogen, NW China. *Journal of Asian Earth Sciences* **2024**, *276*, 106341, doi:https://doi.org/10.1016/j.jseaes.2024.106341.
84. Li, R.-B.; Pei, X.-Z.; Li, Z.-C.; Liu, Z.Q.; Chen, G.-C.; Chen, Y.-X.; Wei, F.H.; Gao, J.M.; Liu, C.J.; Pei, L. Geological characteristics of Late Palaeozoic-Mesozoic unconformities and their response to some

Preprints.org (www.preprints.org) | NOT PEER-REVIEWED | Posted: 18 February 2025 doi:10.20944/preprints202502.1347.v1

signigicant tectonin events in eastern part of Eastern Kunlun. *Earth Science Frontiers* **2012**, *19*, 244-254. (in Chinese with English abstract).
85. Yan, Z.; Bian, Q.-T.; Oleg, A.K.; Igor, I.P.; Li, J.; Wang, Z. Provenance of Early Triassic Hongshuichuan Formation in the southern margin of the East Kunlun Mountains: Constrains from detrital framework, heavy mineral analysis and geochemistry. *Acta Petrologica Sinica* **2008**, *24*, 1068-1078. (in Chinese with English abstract).
86. Hu, C.B.; Li, M.; Zha, X.F.; Gao, X.F.; Li, T. Genesis and Geological Signigicance of Late Paleozoic Mantle-Derived Magmatism in Qimantag, East Kunlun: A Case Study of Intrusion in YingZhuagou. *Earth Science* **2018**, *43*, 4334-4349. (in Chinese with English abstract).
87. Luo, W.X. Petrogenesis and Tectono-thermal history of the plutonic pyroxenite in the middle of East Kunlun orogen, western China. Doctor, China University of Geosciences, Wuhan China, 2012. (in Chinese with English abstract).
88. Xiong, F.-H.; Ma, C.-Q.; Zhang, J.-Y.; Liu, B. LA-ICP-MS zircon U-Pb dating, elements and Sr-Nd-Hf isotope geochemistry of the Early Mesozoic mafic dyke swarms in East Kunlun Orogenic belt. *Acta Petrologica Sinica* **2011**, *27*, 3350-3364. (in Chinese with English abstract).
89. Ren, X.; Dong, Y.; He, D.; Sun, S.; Hauzenberger, C.A.; Zhou, B.; Yue, Y.; Hui, B.; Zhang, B. Petrogenesis and tectonic implications of Late Permian S-type granites in the South Kunlun Belt, northern Tibetan Plateau. *Journal of Asian Earth Sciences* **2022**, *230*, 105204, doi:https://doi.org/10.1016/j.jseaes.2022.105204.
90. Chen, X.-D.; Li, B.; Sun, C.-B.; Zhou, H.-B. Protracted Storage for Calc-Alkaline Andesitic Magma in Magma Chambers: Perspective from the Nageng Andesite, East Kunlun Orogen, NW China. *Minerals* **2021**, *11*, doi:10.3390/min11020198.
91. Xin, W.; Sun, F.-Y.; Zhang, Y.-T.; Fan, X.-Z.; Wang, Y.-C.; Li, L. Mafic–intermediate igneous rocks in the East Kunlun Orogenic Belt, northwestern China: Petrogenesis and implications for regional geodynamic evolution during the Triassic. *Lithos* **2019**, *346-347*, doi:10.1016/j.lithos.2019.105159.
92. Xu, Z.Q.; JIang, M.; Yang, J.S.; Xue, G.Q.; Su, H.P.; Li, H.B.; Cui, J.W.; Wu, C.L.; Liang, F.H. Mantle structure of Qinghai-Tibet Plateau: Mantle plume, mantle shear zone and delamination of lithospheric slab. *Earth Science Frontiers* **2004**, *11*, 329-343. (in Chinese with English abstract).
93. Deng, J.; Wu, Z.; Yang, J.; Zhao, H.; Liu, H.; Lai, S.; Di, Y. Crust-mantle petrological strcucture and deep processes along the Golmud–Ejin Qi geoscience section. *Acta Geophysica Sinica* **1995**, *38*, 130-144. (in Chinese with English abstract).
94. Yu, M.; Feng, C.; Zhao, Y.; Li, D. Genesis of post-collisional calc-alkaline and alkaline granitoids in Qiman Tagh, East Kunlun, China. *Lithos* **2015**, *239*, 45-59, doi:10.1016/j.lithos.2015.08.022.
95. Ding, S.; Huang, H.; Niu, Y.L.; Zhao, Z.D.; Yu, X.H.; Mo, X.X. Geochemistry, geochronology and petrogenesis of East Kunlun high Nb-Ta rhyolites. *Acta Petrologica Sinica* **2011**, *27*, 3603-3614. (in Chinese with English abstract).
96. Gao, Y.B.; Li, W.Y.; Qian, B.; Li, K.; Li, D.S.; He, S.Y.; Zhang, Z.W.; Zhang, J.W. Geochronology, geochemistry and Hf isotopic compositions of the granitic rocks related with iron mineralization in Yemaquan deposit, East Kunlun, NW, China. *Acta Petrologica Sinica* **2014**, *30*, 1647-1665. (in Chinese with English abstract).